Biophysical Journal
Article

Biophysical Society

Diagonally Scanned Light-Sheet Microscopy for Fast Volumetric Imaging of Adherent Cells

Kevin M. Dean,[1,2] Philippe Roudot,[1,2] Carlos R. Reis,[2] Erik S. Welf,[1,2] Marcel Mettlen,[2] and Reto Fiolka[2,*]
[1]Lyda Hill Department of Bioinformatics and [2]Department of Cell Biology, University of Texas Southwestern Medical Center, Dallas, Texas

ABSTRACT In subcellular light-sheet fluorescence microscopy (LSFM) of adherent cells, glass substrates are advantageously rotated relative to the excitation and emission light paths to avoid glass-induced optical aberrations. Because cells are spread across the sample volume, three-dimensional imaging requires a light-sheet with a long propagation length, or rapid sample scanning. However, the former degrades axial resolution and/or optical sectioning, while the latter mechanically perturbs sensitive biological specimens on pliant biomimetic substrates (e.g., collagen and basement membrane). Here, we use aberration-free remote focusing to diagonally sweep a narrow light-sheet along the sample surface, enabling multicolor imaging with high spatiotemporal resolution. Further, we implement a dithered Gaussian lattice to minimize sample-induced illumination heterogeneities, significantly improving signal uniformity. Compared with mechanical sample scanning, we drastically reduce sample oscillations, allowing us to achieve volumetric imaging at speeds of up to 3.5 Hz for thousands of Z-stacks. We demonstrate the optical performance with live-cell imaging of microtubule and actin cytoskeletal dynamics, phosphoinositide signaling, clathrin-mediated endocytosis, polarized blebbing, and endocytic vesicle sorting. We achieve three-dimensional particle tracking of clathrin-associated structures with velocities up to 4.5 μm/s in a dense intracellular environment, and show that such dynamics cannot be recovered reliably at lower volumetric image acquisition rates using experimental data, numerical simulations, and theoretical modeling.

INTRODUCTION

Fluorescence microscopy is the method of choice for analyzing cellular heterogeneity (1), the spatiotemporal dynamics of signal transduction (2), and the evolution of molecular architectures (3). However, the absorption of light by fluorophores and electronically conjugated intracellular constituents (e.g., NADH and flavins) produces chemically reactive species that compromise cellular health and degrade image contrast (4). Thus, to minimize photobleaching and phototoxicity, the excitation light should ideally be 1) kept at low intensities, 2) restricted to the focal plane that is being imaged, and 3) fluorescence should be efficiently captured. These three criteria are fulfilled by light-sheet fluorescence microscopy (LSFM), which illuminates only the part of the sample that is in focus and significantly reduces sample irradiance (5). Consequently, LSFM has enabled unprecedented long-term functional imaging of embryogenesis and neurotransmission in small and sufficiently transparent animals, including *Drosophilia melanogaster*, *Danio rerio*, and *Caenorhabditis elegans* (6).

Typically, one-dimensional (1D) and two-dimensional (2D) Gaussian beams are used to generate a light-sheet, as such beams most effectively confine the excitation power to the focal plane. An obvious drawback of Gaussian optics is that with an increasing field of view (FOV), restricted by ~2 Rayleigh lengths of the beam, the beam waist grows and degrades the axial resolution (7). Various illumination strategies have been proposed to overcome this inherent trade-off between axial resolution and FOV, including Bessel beams and their coherent superposition (8–12), Airy beams (13), extended focusing (14,15), fusion of multiple volumetric data sets (16,17), and scanning a narrow light-sheet in the image plane (18). Although all of these techniques extend the FOV for a given axial resolution, they do so by drastically reducing illumination confinement. Consequently, important advantages of LSFM are lost, including the reduction of volumetric sample exposure and the minimization of photobleaching and phototoxicity. To simultaneously achieve high excitation confinement and axial resolution, it is preferable to illuminate the sample with the shortest light-sheet possible, regardless of the type of light-sheet (e.g., Gaussian, Bessel, or Airy) used.

Submitted November 2, 2015, and accepted for publication January 28, 2016.

*Correspondence: reto.fiolka@utsouthwestern.edu
Kevin M. Dean and Philippe Roudot contributed equally to this work.

Editor: Paul Wiseman.
http://dx.doi.org/10.1016/j.bpj.2016.01.029

Many mammalian cell types adopt thin morphological profiles when adhered to rigid planar substrates (e.g., optical coverslips). If such a sample is mounted at 45° relative to the optical axes of the illumination and detection optics, a narrow light-sheet is sufficient to illuminate even the tallest part of the cell (Fig. 1 *A*). Furthermore, this arrangement is favorable for water-dipping objectives, as both the illumination and detection light paths are not aberrated by the glass coverslip. Nevertheless, for adherent cells oriented at 45°, a scan in the *Z*-direction is accompanied by a lateral shift of the sample relative to the beam waist in the *Y* direction (Fig. 1 *A*), necessitating a longer light-sheet at the cost of decreased axial resolution and/or illumination confinement. This problem can be overcome by diagonally scanning the sample itself through the beam waist (9). However, at rapid imaging speeds, sample scanning may perturb the biological sample, and each image slice has to be computationally shifted (deskewed) to its proper position in the three-dimensional (3D) image volume (11). As subpixel shifts are required, interpolation of the data cannot be avoided, resulting in local smoothing of the data and alteration of the signal statistics.

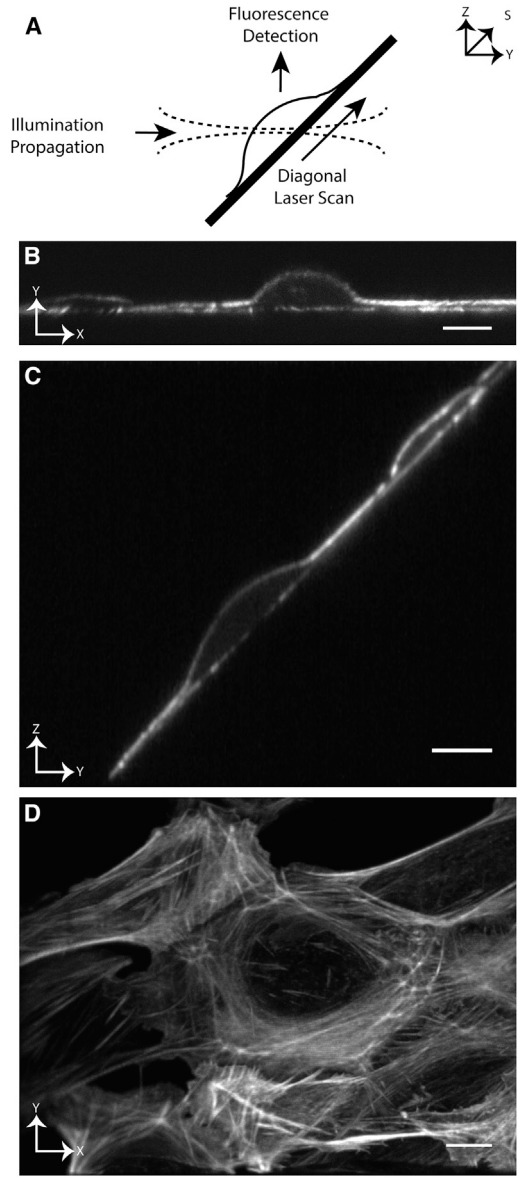

FIGURE 1 (*A*) Schematic of DiaSLM. A dithered Gaussian lattice propagating in the *Y*-direction illuminates a cell oriented at 45°, and fluorescence is imaged in an orthogonal direction. The illumination beam is scanned diagonally in the *S*-direction along the coverslip, and an image is acquired at each *Z* plane. The beam length is configured to encompass the tallest region of the cell (e.g., the nucleus, ~11 μm at FWHM). (*B*) Image of U2OS cells expressing CyOFP-Tractin, acquired at an intermediate *Z* plane. (*C*) A single plane in *YZ*, showing the 45° sample geometry and high degree of optical sectioning. (*D*) *XY* maximum intensity projection of the same U2OS cells expressing CyOFP-Tractin. Scale bar, 10 μm.

Previously, we reported a variant of LSFM, referred to as axially swept light-sheet microscopy (ASLM), that achieved isotropic sub-400 nm resolution throughout large imaging volumes (160 × 160 × 100 μm^3) (18). In ASLM, a narrow light-sheet is swept along its propagation path (*Y*-direction) with a remote focusing scan mechanism and only the in-focus region is imaged. However, when equipped with galvanometric mirrors that scan the beam in both *Z* and *X*, the illumination train for ASLM is also capable of translating a light-sheet arbitrarily in 3D, including along a coverslip oriented at 45° relative to the optical axes. We exploited this capability to create a new imaging mode for ASLM, which we refer to as diagonally swept light-sheet microscopy (DiaSLM), that allows rapid multicolor and volumetric imaging (3.5 Hz) of cells on 2D surfaces. Since the light-sheet is placed at the optimal position in both the *Z*- and *Y*-directions for every Z-slice, sample scanning (and thus mechanical perturbation of the sample) is unnecessary. This scheme provides true 3D imaging in the sense that the raw sample information is in its proper Euclidean reference frame without the need for any signal-altering computational processing. Because our light-sheet is free of side lobes that propagate beyond the detection objective depth of focus, the raw data are devoid of out-of-focus blur. Thus, in contrast to most high-resolution LSFM techniques (9,11,14,16,19), computational deconvolution or reconstruction of the data is unnecessary, the statistical moments of the data are preserved, and the data can be viewed and analyzed in their raw form.

Here, we demonstrate potential applications of DiaSLM by volumetrically imaging rapid intracellular dynamics in live-cells for thousands of Z-stacks. These processes include actin and microtubule dynamics, clathrin-mediated endocytosis (CME), phosphoinositide signaling, endocytic trafficking of transferrin, membrane protrusions, ruffling, and polarized blebbing. We also perform 3D particle tracking of densely populated clathrin-coated structures with velocities up to 4.5 μm/s. Using simulations and a mathematical model that relates particle motion, particle density, and the volumetric image acquisition rate, we show that such dynamics cannot be reliably estimated below a 3D image

acquisition rate of 3.1 Hz. Lastly, we perform mechanically nonperturbative imaging of cells on top of thick extracellular matrices (ECMs).

MATERIALS AND METHODS

Microscope setup

The microscope configuration is presented in Fig. S1 in the Supporting Material. Two modifications of ASLM (18) were introduced to enable greater illumination intensity stability and uniformity. Illumination stability was improved by modulating the laser amplitude with a temperature-stabilized acousto-optical tunable filter (AOTFnC-400.650-TN; AA Opto-Electronic, Orsay, France). Illumination uniformity was improved by generating a lattice of Gaussian beams at the sample plane and dithering the lattice in the *X*-direction with a galvanometric mirror conjugate to the back-pupil plane of the excitation objective. The Gaussian lattice was generated with a custom-built binary amplitude grating (20% transmission, 60 μm pitch; Photo Sciences, Torrance, CA) conjugated to the sample plane. The grating was designed so that for both excitation wavelengths (488 and 560 nm), five diffraction orders (0, $\pm$1, and $\pm$2) fit into the back pupil of the excitation objective (40×, 0.8 NA; Nikon Instruments, Melville, NY). A low-spatial-duty cycle was selected to strengthen the higher diffraction orders relative to the zeroth diffraction order, thereby improving the illumination homogenization. The X-galvo (6210HSM40B; Cambridge Technologies, Bedford, MA) was conjugated to the Z-galvo (6210HSM40B; Cambridge Technologies) with a pair of 60 mm achromatic doublets (AC254-060A; ThorLabs, Newton, NJ). All downstream components were identical to those reported previously (18), with the exception of the scan lens (S4LFT4375; Sill Optics, Wendelstein, Germany), which was inadvertently reported to have a focal length of 60 mm (it is actually 80.2 mm).

At an NA of 0.8 (the maximum of our excitation objective), the dithered Gaussian lattice had a 20% and 30% larger beam waist and propagation length (defined as 2 Rayleigh lengths of the beam), respectively, than a canonical 1D Gaussian beam. This is because the higher diffraction orders ($\pm$1 and $\pm$2) have a lower effective NA than the zeroth-order beam. In this work, we did not use the full NA of the illumination objective, a parameter that was controlled by a variable slit aperture (Fig. S1 *A*). By adjusting the slit width, we could arbitrarily control the NA of the illumination beam. Here, we routinely set the full width half maximum (FWHM) of the beam waist and propagation length to ~800 nm and ~11 μm, respectively, in the sample plane of the microscope. Using 100 nm fluorescent spheres (Fluoresbrite Plain YG; Polysciences, Warrington, PA), the axial and lateral resolution was found to be 725 $\pm$ 29 nm and 379 $\pm$ 18 nm, respectively. Because the detection path remained unchanged, the lateral resolution is the same as that reported for ASLM (18).

For optimal high-speed and high-resolution imaging, vibrations were identified with an accelerometer (41A19-1032; Meggitt Sensing Systems, Irvine, CA), an IEPE data acquisition system (cDAQ-9171 and NI 9234; National Instruments, Austin, TX), and custom software (LabView; The MathWorks, Natick, MA). Primary vibrations included the 488 nm laser fan (95 and 661 Hz, Sapphire; Coherent, Santa Clara, CA), camera fan (67 and 337 Hz, Flash 4.0; Hamamatsu, Bridgewater, NJ), piezo driver (86, 123, 617, and 863 Hz; E-509; Physik Instrumente, Auburn, MA), and building (2.5 Hz). With the exception of those induced by the building, vibrations were remedied by turning off the laser and camera fans, providing water cooling to the camera (ThermoCube 300; Solid State Cooling Systems, Wappingers Falls, NY), and removing the piezo driver from the optical table.

Sample scan experiments

To evaluate sample scanning, an objective scan unit (P-726.1CD; Physik Instrumente) was attached to a 3D stage (MP-285; Sutter Instruments) for sample positioning. Instead of the objective, a short lens tube (SM1L01; ThorLabs) was mounted to the piezo scanner with a thread adaptor. At the end of the lens tube, an SM1 threaded cage plate (CP08; ThorLabs) was attached. Our custom-fabricated 5 mm coverslip mounting unit (White Glove Machining, Upper Marlboro, MD) was mounted to the cage plate with a 0.75-inch-long 0.5-inch-diameter stainless steel optical post (TR075; ThorLabs). To evaluate whether the sample mount itself had measurable mechanical oscillations, we imaged 200 nm fluorescent microspheres that had adhered to glass coverslips in sample scanning and DiaSLM modes.

Sample preparation

All samples were positioned at 45° relative to the excitation and detection axes. Cellular imaging was performed on #1 thickness glass substrates (CS-5R; Warner Instruments) within a custom low-profile coverslip mounting system (White Glove Machining). A CAD drawing of the sample holder and its positioning relative to the objectives is shown in Fig. S2. ECM-based imaging was performed identically, with the exception that the coverslip was recessed 2 mm to provide a thick substrate. This allowed us to keep the cells far away from stiff surfaces, decreasing the likelihood of alterations to their mechanical microenvironment. ECMs were prepared by neutralizing pepsinized bovine collagen I at a final concentration of 2 mg/mL (Corning, Corning, NY). For the 50:50 collagen matrigel matrix, equal parts of matrigel and 2 mg/mL collagen I solution were mixed rapidly during polymerization of the matrix.

SK-MEL2 melanoma cells overexpressing human clathrin light chain A (CLCa) fused to TagRFP-T (20) have been previously described (21). We labeled F-actin in these cells by infecting them with lentivirus encoding Tractin-EGFP, a peptide that contains residues 9–52 of the F-actin-binding enzyme ITPKA (22). After infection, the cells were placed under selection with 0.1 mg/mL puromycin for 10 days, sorted for cells positive for both red and green expression, and amplified in the absence of puromycin. For imaging, cells were trypsinized and seeded at ~75% confluency directly on uncoated flame-sterilized coverglass. Cells were imaged 18–24 h after seeding. Spontaneously arising retinal pigment epithelial (ARPE)-19 cells were infected with retrovirus generated from a pMIEG3 vector encoding EGFP-CLCa, as previously described (23). Then, 10^5 cells were seeded per well in a six-well plate containing 5 mm uncoated coverslips with Dulbecco's modified Eagle medium/F12 containing 10% fetal bovine serum. MV3 cells were grown in Dulbecco's modified Eagle medium supplemented with 10% fetal calf serum and 0.1% antibiotic, and stably transfected with the GFP-AktPH biosensor in a retroviral vector as described previously (24). Osteosarcoma cells (U2OS) were maintained in McCoy's 5A medium with 10% fetal bovine serum and 0.2% antibiotic-antimycotic, and the filamentous actin was labeled with lentivirus encoding CyOFP-Tractin. CyOFP is a novel cyan-excitable orange fluorescent protein with peak excitation and emission at 505 and 588 nm, respectively, and will be described elsewhere.

RESULTS

The concept of DiaSLM is schematically shown in Fig. 1 *A* and a technical drawing of the microscope is presented in Fig. S1 *A*. The sample, placed at 45° relative to the excitation and detection axes, is illuminated with a dithered Gaussian lattice (see below; beam propagation length ~11 μm, beam waist ~800 nm; Fig. S1, *B* and *C*) propagating in the *Y*-direction (25). When viewed on a camera, the cell thus appears as a narrow optical section, as shown in Fig. 1 *B*. To generate 3D data, the dithered light-sheet is scanned diagonally along the coverslip and an optical

section of the cell is acquired for each plane in the *Z*-direction. Scanning of the illumination beam in the *Y*- and *Z*-directions is achieved with aberration-free remote focusing (18,26,27) and a galvanometric mirror, respectively. The detection objective is synchronously stepped with a piezo actuator.

Because the light-sheet is free of side lobes, a high degree of optical sectioning (i.e., the ability to reject light originating from outside of the detection objective's depth of focus) is achieved, as shown in a *YZ* cross-section (Fig. 1 *C*). Alternatively, projecting the data along the *Z* axis provides a convenient view of the entire cell, albeit rotated 45° off-axis from the coverslip (Fig. 1 *D*). Affine transformation of the data can reorient the sample into the more familiar epifluorescence perspective (e.g., normal to the coverslip), but at the cost of interpolating voxel intensities.

The same image volume could be acquired with ASLM (18), but for this particular sample geometry, DiaSLM offers two important advantages. First, because the time-averaged Gaussian lattice in DiaSLM is approximately stationary during each camera exposure, the effective pixel dwell time is drastically longer (~30× for a 512 × 512 image). Second, in DiaSLM, the remote focusing piezo actuator makes only one sweep during the acquisition of an entire Z-stack, whereas in ASLM it makes one sweep per acquired image plane (see schematic, Fig. S3). Therefore, the bandwidth requirements of the remote focusing piezo are relaxed by ~2 orders of magnitude. Together, these advantages result in improved sensitivity, decreased sample irradiance (e.g., 0.3–30 μW in the back pupil of the excitation objective), diminished photobleaching and phototoxicity, and image acquisition rates approaching the camera-readout limited regime (400 planes per second for a 512 × 512 image). Consequently, DiaSLM enables routine multicolor observation of cells in 3D for thousands of Z-stacks at a volumetric image acquisition rate of up to 3.5 Hz, without stereotypic phototoxic signatures (Movie S1).

The effective pixel dwell time is a key parameter for imaging sensitivity in LSFM (11), but it must be balanced with illumination uniformity. For example, a 1D light-sheet formed by a cylindrical lens enables instantaneous illumination of the entire FOV (and thus the highest-illumination duty cycle). However, such a beam geometry is prone to shadow artifacts that arise from sample heterogeneity and imperfections in the optical train (25). The evenness of illumination can be greatly enhanced by rapidly sweeping a 2D Gaussian beam across the FOV to generate a time-averaged light-sheet. The improvement in illumination uniformity arises because a 2D Gaussian beam fills a much larger solid angle than a beam generated from a cylindrical lens. However, sweeping comes at the cost of a drastically decreased illumination duty cycle (9,28). Alternatively, a 1D illumination beam can be rotated in the sample plane, but, for short beams, this results in an unacceptable amount of out of focus illumination and blur (25). In DiaSLM, we balance the spatial duty cycle and illumination heterogeneity by generating a discrete set of laterally superimposed 2D Gaussian beams, which we refer to as a Gaussian lattice. We produce this lattice by placing a custom amplitude grating conjugate to the sample plane in the illumination path (Fig. S1). The Gaussian lattice is dithered in the *X*-direction with a galvanometric mirror to produce a time-averaged light-sheet with greatly improved illumination homogeneity (Fig. S4).

As a result of the rapid image acquisition rate and sensitive detection, DiaSLM enabled us to image a wide variety of fast-timescale biological events in 3D, including GFP-AktPH, a biosensor that reports on local phosphatidylinositol-3-kinase (PI3K) activity. Typically, such translocation biosensors must be imaged by total internal reflection fluorescence (TIRF) microscopy (29), which is limited to the ventral surface of cells and precludes observation of large-scale membrane ruffles (24). We volumetrically imaged GFP-AktPH in MV3 melanoma cells and observed heightened PI3K activity in membrane ruffles (Fig. 2, *A* and *B*; Movies S2 and S3). Although PI3K activity is necessary for membrane ruffling and accordingly has been observed in ruffles close to adhesive surfaces via TIRF or at indeterminate locations via epifluorescence (30–32), this is, to our knowledge, the first direct observation of PI3K activity in dorsal membrane ruffles. We also observed the formation of transverse arcs, specialized actin filaments involved in cell migration (Fig. 2 *C*), and the dynamics of other actin cytoskeleton-related structures (e.g., lamellipodium) in U2OS osteosarcoma cells (33). Furthermore, by labeling microtubule +TIPs with EB3-mNeonGreen, DiaSLM clearly resolved microtubule polymerization and centrosome position in 3D (Fig. 2 *D*; Movie S4).

We also imaged MV3 melanoma cells expressing GFP-Tractin, which binds to filamentous actin, undergoing polarized blebbing (Fig. 3 *A*; Movie S5). Despite cellular heterogeneity (some cells spread and generated fibroblast-like morphological profiles (e.g., Fig. 2 *B*), many cells exhibited a stereotypical polarized amoeboid phenotype (34). Here, blebbing events were observed opposite to a stable uropod (35), with blebs and membrane appearing to flow backward toward the uropod. In some cases, the uropod was observed on the dorsal surface of the cell, and blebbing proceeded around the entire cell perimeter (data not shown). Because of the high temporal sampling (2.86 Hz), we were able to clearly resolve separation of the membrane from the actin cortex, rapid hemispherical expansion of the membrane, and polymerization of a nascent F-actin cortex within the newly protruded region (*arrows* in Fig. 3 *B*; Movie S6).

Because DiaSLM is based upon refractive optical elements, it is capable of operating in a simultaneous multicolor or pulse-interleaved illumination mode. In cases where fluorophore crosstalk is negligible, simultaneous multicolor illumination maximizes the image acquisition

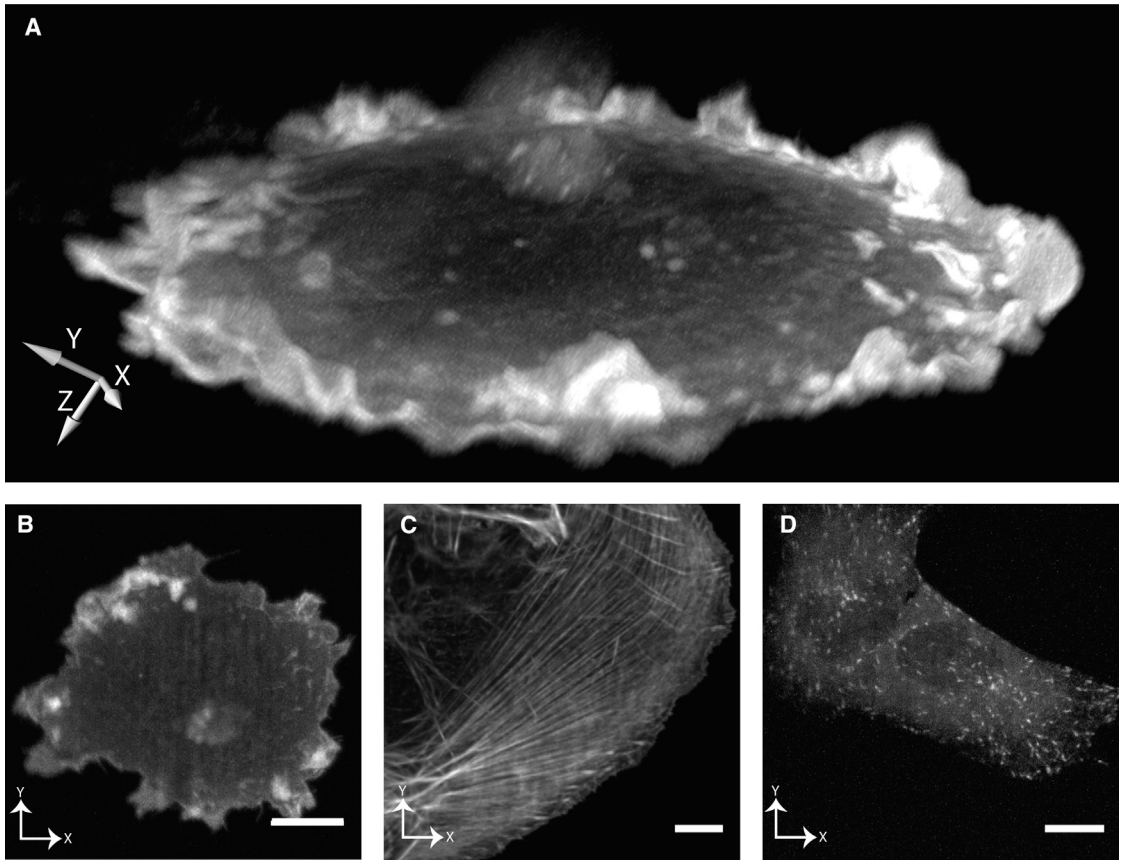

FIGURE 2 Dynamic signal transduction and cytoskeletal reorganization imaged in 3D with DiaSLM. (*A*) Volume rendering of a GFP-AktPH biosensor in a MV3 melanoma cell, with enhanced phosphatidylinositol localization in active membrane ruffles. (*B*) Maximum intensity projection of another MV3 cell expressing the GFP-AktPH biosensor. (*C*) Transverse contractile actin stress fibers in an osteosarcoma U2OS cell labeled with tractin-CyOFP. (*D*) Microtubule +TIP dynamics in adjacent osteosarcoma U2OS cells labeled with EB3-mNeonGreen. Scale bar, 10 μm.

rate and enables the application of advanced computer vision frameworks, including econometric analysis of biological fluctuations and causality in signal transduction (2,36,37). In contrast, the pulsed-interleaved mode minimizes fluorescence crosstalk but introduces a small temporal delay between the acquisitions of each color channel.

To demonstrate these imaging modes, we first imaged the dynamics of CME and the filamentous actin cytoskeleton using the simultaneous image acquisition mode in SK-MEL-2 melanoma cells (Fig. 4, *A–C*; Movie S7). The role of the actin cytoskeleton in CME remains controversial and is an active area of research, with investigators reporting

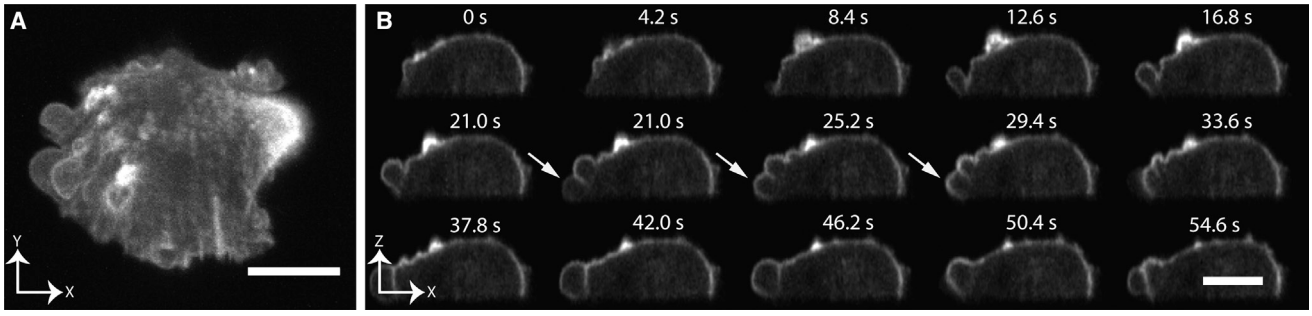

FIGURE 3 Volumetric imaging at 2.86 Hz of an MV3 cell labeled with GFP-Tractin undergoing polarized blebbing. (*A*) *XY* maximum intensity projection. Blebs initiate adjacent to the coverslip on the left and flow toward a stable uropod, located in the upper right. (*B*) Montage of bleb formation and cortical flow. Every 12th time point of a single *XZ* cross section is shown. Arrows indicate membrane detachment from the actin cortex, polymerization of a nascent cortical actin meshwork, and flow toward the uropod (not visible in this cross section). Scale bar, 10 μm.

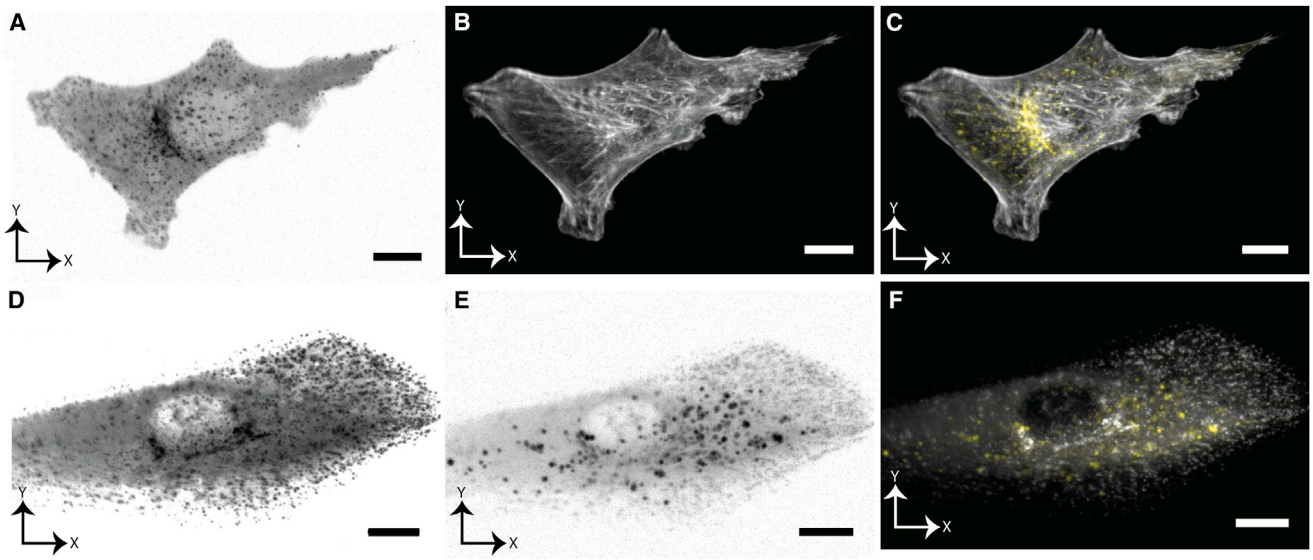

FIGURE 4 Volumetric multicolor imaging of the actin cytoskeleton, CME, transferrin uptake, and endosomal recycling. (*A* and *B*) *XY* maximum intensity projections of an SK-MEL-2 melanoma cell labeled with (*A*) CLCa-TagRFP-T and (*B*) EGFP-Tractin (image shown with a gamma correction of 0.7). (*C*) Merged color channels shown in (*A*) and (*B*). Images were acquired in a pulse-interleaved multicolor imaging mode at 0.19 Hz. (*D* and *E*) *XY* maximum intensity projections of human ARPE-19 cells labeled with (*D*) CLCa-EGFP and (*E*) Alexa Fluor 568-transferrin. (*F*) Merged color channels shown in (*D*) and (*E*). Images were acquired in a simultaneous multicolor imaging mode at 0.36 Hz. Scale bar, 10 μm.

contradictory observations depending on the cell type. Boulant et al. (38) suggested that actin's main function during CME may be to counteract membrane tension, which hinders clathrin-coated pits from acquiring curvature. Since membrane tension depends on cellular adhesion and contractility, studying CME on both dorsal and ventral cell surfaces could provide significant insight into the molecular regulation and kinetics of CME.

We also imaged CLCa-EGFP-expressing cells in pulse-interleaved mode together with fluorescently labeled transferrin, which is transported into the cell by receptor-mediated endocytosis and is commonly used as a marker for CME. This allowed us to observe sites of transferrin uptake and their relation to CLCa-EGFP. In nonpolarized RPE cells, intracellular vesicles containing transferrin appeared to undergo periods of local diffusion followed by short bursts of rapid transport (Fig. 4, *D–F*; Movie S8). We also observed similar dynamics for clathrin-associated structures in polarized epithelial cells when we imaged Caco-2 human colon carcinoma cells, which adopt a columnar epithelial-tissue-like morphology. Biologically, these fast motions likely reflect large-scale motor-protein-driven transport along microtubules (39). Although the function of these clathrin-associated vesicles remains poorly understood, their rapid intracellular velocities are 1–2 orders of magnitude faster than the dynamics of clathrin-coated pits observed on the cell membrane (40).

In an effort to quantify the fast intracellular transport of the clathrin-associated structures, we performed single-particle tracking with the automatic and locally adaptive u-track software (41,42). At a volumetric image acquisition rate of 3.5 Hz, we were able to robustly track active transport of particles with velocities between 2.2 and 4.5 μm/s in a dense field of locally diffusing objects (0.7–1.9 objects per μm^3, near the plasma membrane and Golgi apparatus, respectively; see Figs. 5, *A* and *B* and S5; Movie S9). However, despite optimization of the tracking parameters, at a volumetric image acquisition rate of 2.3 Hz, automated particle tracking failed (Movie S10; Note S1 in the Supporting Material).

To investigate the capacity of our microscope to improve automated particle tracking robustness in dense intracellular environments, we simulated the observed active transport of diffraction-limited structures in a field of confined particles with local densities ranging from 0.1 to 4 particles per μm^3 (Note S2 in the Supporting Material). To evaluate tracking robustness, we compared the particle trajectories with the simulation ground truth. In agreement with experimental observations, the simulations suggested that robust tracking was only feasible at volumetric image acquisition rates greater than 3 Hz (Fig. 5 *C*; Movie S11), even in the sparsest scenario (0.1 particles per μm^3).

We also investigated the theoretical requirements for reliable 3D particle tracking by developing a mathematical model that deduces the relationship between the volumetric image acquisition rate, local object density, and object motion while considering the robustness and predictive capacity of conventional tracking algorithms (Note S3 in the Supporting Material). For a single actively transported particle, geometric considerations show that the volumetric

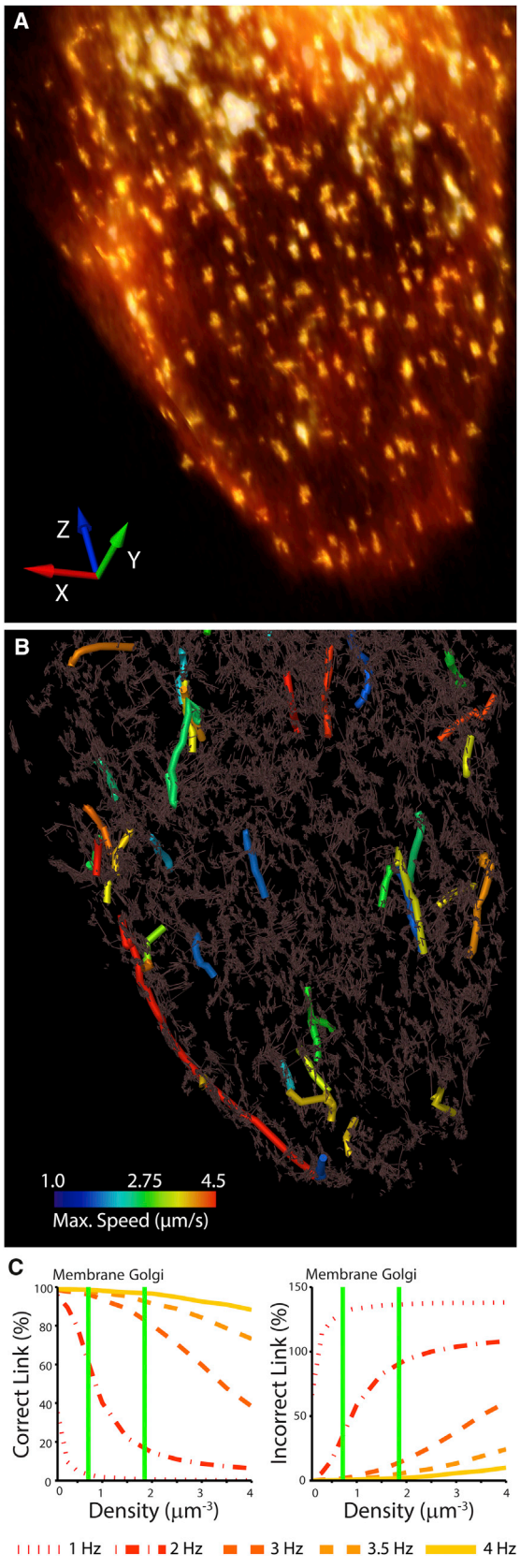

FIGURE 5 Volumetric imaging (3.5 Hz) of CLCa dynamics in Caco-2 epithelial cells. (*A*) Volume rendering of Caco2 epithelial cell expressing CLCa-EGFP. To aid in the visualization of dim structures, the raw data are merged with the adaptively thresholded mask used for particle detection. (*B*) Cumulative plot of clathrin tracks. Confined motions, representing CLCa at sites of endocytosis, are in grayscale. Intracellular clathrin-associated particles undergoing active transport, identified as particles with a diffusion coefficient greater than 100 $\mu m^3/s$, are pseudocolored according to their maximum velocity. (*C*) Numerical simulations and tracking performance as a function of particle density and the volumetric image acquisition rate. Performance is only measured on tracks undergoing active transport (>2.2 μm/s), and percentages are relative to the simulation ground truth.

image acquisition rate must increase linearly with the minimum particle velocity, with the square root of the particle's instantaneous acceleration, and with the cube root of the particle density. Thus, given the densities observed for the intracellular clathrin-associated structures in Fig. 5, a volumetric image acquisition rate of at least 3.1 Hz is necessary to accurately track particle dynamics without introducing false positives. This prediction was supported by further numerical simulations, which evaluated tracking performance at volumetric image acquisition rates between 0.1 and 6.0 Hz (Fig. S6). These data underscore the importance of Nyquist sampling in both space and time to mitigate analytical artifacts (43). This model also provides us with a prediction of the required acquisition speed for a given biological process of interest and the density of labeled intracellular objects.

Lastly, in an attempt to more faithfully replicate the chemical and mechanical properties experienced by cells in vivo, we imaged human bronchial epithelial and U2OS cells on top of pliant ECMs. Indeed, the mechanochemical properties of the ECM have significant effects on cell morphology, cell fate, and cancer progression (44–46). However, the pliant nature of the ECM prohibits rapid sample scanning, as image quality is degraded by oscillations introduced into the sample (Fig. 6 *A*). These oscillations arise from the ECM and not from the sample holder, as we verified by imaging beads on a rigid glass coverslip (Fig. S7). Since DiaSLM keeps the sample stationary and diagonally scans the illumination beam without external mechanical perturbation, we were able to rapidly image the ECM without introducing sample oscillations (Fig. 6 *B*). Through this approach, we were able to observe cytoskeletal dynamics in a dense layer of nonpolarized RPE cells (Fig. 6 *C*; Movie S12) and the cell-spreading behavior of a U2OS cell (Fig. 6 *D*; Movie S13). Cell spreading is a mechanosensitive process and is one of the principal steps in polarity establishment and the adoption of a cell-type-specific morphological output. Thus, with DiaSLM, one may now study cellular behavior with high spatiotemporal resolution in more physiological microenvironments.

DISCUSSION

We have introduced DiaSLM as a method for rapid and efficient 5D (*X*, *Y*, *Z*, time, and wavelength) imaging of

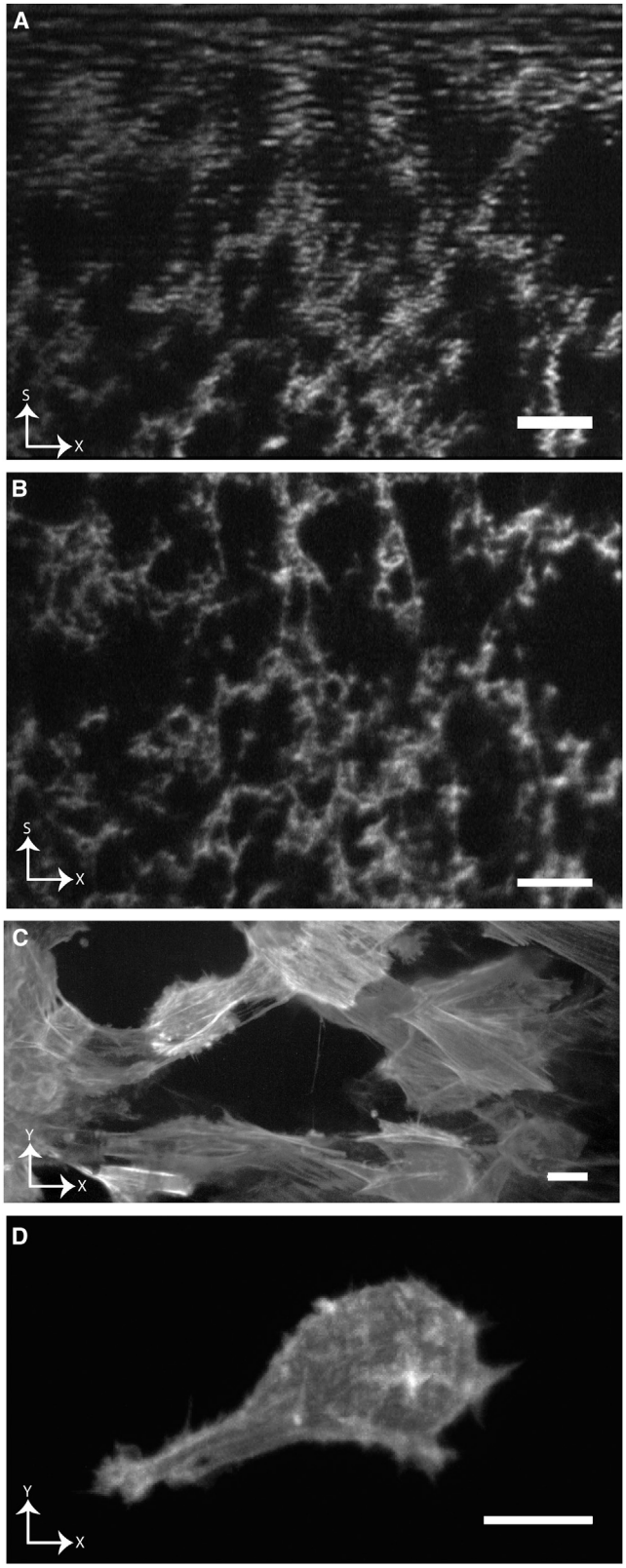

FIGURE 6 High-speed imaging on pliant ECMs. (*A*) Rapid sample scanning induces vibrations in the collagen matrix that degrade image quality. Each plane was acquired in 5 ms and the final data were deskewed and affine transformed for visualization. A maximum intensity projection over a shallow volume is shown. (*B*) DiaSLM imaging of the same collagen area as in (*A*). Each plane was acquired in 5 ms and the final data were affine transformed for visualization. A maximum intensity projection over a shallow volume is shown. (*C*) *XY* maximum intensity projection of a confluent monolayer of nonpolarized human bronchial epithelial cells on an ECM consisting of equal parts of type II collagen (final concentration, 1 mg/mL) and matrigel. Cells were labeled with Tractin-GFP and volumetrically imaged at 0.17 Hz. (D) *XY* maximum intensity projection of a single U2OS cell undergoing cell spreading on a 2 mg/mL collagen matrix, volumetrically imaged at 1.38 Hz. Scale bar, 10 μm.

adherent cells, and demonstrated its potential by volumetrically resolving cellular processes at image acquisition rates up to 3.5 Hz for thousands of Z-stacks. In contrast to sample scanning, DiaSLM avoids mechanical perturbation of the sample, which is particularly important for biological studies on soft substrates, including reconstituted ECM. However, faster acquisition rates will be necessary to follow some biological processes. For example, even at 3.5 Hz, some intracellular clathrin-coated vesicles proved particularly challenging for robust 3D tracking.

Several strategies can be used to accelerate the volumetric imaging rate beyond 3.5 Hz. As currently implemented in DiaSLM, Z-stepping of the detection objective is rate limiting. This is because the mass of the objective is approximately two orders of magnitude greater than the mass of the remote focusing mirror unit. Thus, to further improve temporal resolution, one must eliminate the objective's physical movement. This can be achieved with the use of an electrotunable lens or a deformable mirror that refocuses the focal plane onto the camera (47), wavefront coding (48,49), or aberration-free remote focusing in the detection arm of the microscope (26,27). With these additions, and by adding a faster actuator for the remote focusing mirror (27), video-rate DiaSLM imaging should be feasible with optimal fluorescent probes, labeling strategies, and scientific cameras with accelerated readout speeds (50).

In summary, DiaSLM complements ASLM for rapid and efficient volumetric imaging of adherent cells on 2D surfaces. Owing to rapid progress in high-resolution LSFM, biological processes that hitherto have been only accessible to 2D imaging (e.g., TIRF microscopy) can now be performed in 3D, thereby greatly expanding the number of biological questions that can be addressed. Furthermore, DiaSLM enables biologists to move beyond the optical coverslip and into more physiologically meaningful environments. Thus, owing to its mechanical noninvasiveness, efficient use of short illumination beams, high optical sectioning strength, and simultaneous multicolor capability, as well as the fact that raw data can be visualized and analyzed directly in their raw form, DiaSLM is an enabling technique that will accelerate biological research.

SUPPORTING MATERIAL

Supporting Materials and Methods, seven figures, and thirteen movies are available at http://www.biophysj.org/biophysj/supplemental/S0006-3495(16)00139-9.

AUTHOR CONTRIBUTIONS

K.M.D. and R.F. conceived and built the microscope, analyzed the data, and wrote the manuscript. K.M.D., E.S.W., and R.F. performed the experiments. K.M.D., C.R.R., M.M., and R.F. designed the biological experiments. P.R. performed dynamic resolution modeling, simulations, and 3D particle detection and tracking.

ACKNOWLEDGMENTS

We thank the BioHPC team at the University of Texas Southwestern Medical Center for providing the infrastructure and support for analysis of large data sets, Dr. Dick McIntosh (University of Colorado Boulder) for kindly providing us with U2OS cells, Dr. Kim Reed for administrative and scientific support, and Dr. Sandra Schmid for helpful discussion.

This work was supported by the Cancer Prevention Research Institute of Texas (R1225 to Dr. Gaudenz Danuser), the National Institutes of Health (GM73165 to Drs. Gaudenz Danuser and Sandra Schmid and F32GM117793 to K.M.D.), and the Human Frontier Science Program (fellowship LT000954/2015 to P.R.). The content of the manuscript is solely the responsibility of the authors and does not represent the official views of the National Institutes of Health, Cancer Prevention Research Institute of Texas, or Human Frontier Science Program. The LabView software used to control the microscope was custom developed by Coleman Technologies, building on a core set of functions licensed from the Howard Hughes Medical Institute's Janelia Farm Research Campus.

REFERENCES

1. Schubert, W., B. Bonnekoh, …, A. W. M. Dress. 2006. Analyzing proteome topology and function by automated multidimensional fluorescence microscopy. *Nat. Biotechnol.* 24:1270–1278.
2. Machacek, M., L. Hodgson, …, G. Danuser. 2009. Coordination of Rho GTPase activities during cell protrusion. *Nature.* 461:99–103.
3. Van Engelenburg, S. B., G. Shtengel, …, J. Lippincott-Schwartz. 2014. Distribution of ESCRT machinery at HIV assembly sites reveals virus scaffolding of ESCRT subunits. *Science.* 343:653–656.
4. Vegh, R. B., K. B. Bravaya, …, K. M. Solntsev. 2014. Chromophore photoreduction in red fluorescent proteins is responsible for bleaching and phototoxicity. *J. Phys. Chem. B.* 118:4527–4534.
5. Scherf, N., and J. Huisken. 2015. The smart and gentle microscope. *Nat. Biotechnol.* 33:815–818.
6. Huisken, J., J. Swoger, …, E. H. Stelzer. 2004. Optical sectioning deep inside live embryos by selective plane illumination microscopy. *Science.* 305:1007–1009.
7. Born, M., E. Wolf, and E. Hecht. 2000. Principles of optics: electromagnetic theory of propagation, interference and diffraction of light. *Phys. Today.* 53:77–78.
8. Fahrbach, F. O., and A. Rohrbach. 2012. Propagation stability of self-reconstructing Bessel beams enables contrast-enhanced imaging in thick media. *Nat. Commun.* 3:632.
9. Planchon, T. A., L. Gao, …, E. Betzig. 2011. Rapid three-dimensional isotropic imaging of living cells using Bessel beam plane illumination. *Nat. Methods.* 8:417–423.
10. Zhao, M., H. Zhang, …, L. Peng. 2014. Cellular imaging of deep organ using two-photon Bessel light-sheet nonlinear structured illumination microscopy. *Biomed. Opt. Express.* 5:1296–1308.
11. Chen, B. C., W. R. Legant, …, E. Betzig. 2014. Lattice light-sheet microscopy: imaging molecules to embryos at high spatiotemporal resolution. *Science.* 346:1257998.
12. Fahrbach, F. O., and A. Rohrbach. 2010. A line scanned light-sheet microscope with phase shaped self-reconstructing beams. *Opt. Express.* 18:24229–24244.
13. Vettenburg, T., H. I. C. Dalgarno, …, K. Dholakia. 2014. Light-sheet microscopy using an Airy beam. *Nat. Methods.* 11:541–544.
14. Dean, K. M., and R. Fiolka. 2014. Uniform and scalable light-sheets generated by extended focusing. *Opt. Express.* 22:26141–26152.
15. Zong, W., J. Zhao, …, L. Chen. 2014. Large-field high-resolution two-photon digital scanned light-sheet microscopy. *Cell Res.* 25:254–257.
16. Wu, Y., P. Wawrzusin, …, H. Shroff. 2013. Spatially isotropic four-dimensional imaging with dual-view plane illumination microscopy. *Nat. Biotechnol.* 31:1032–1038.
17. Gao, L. 2015. Extend the field of view of selective plan illumination microscopy by tiling the excitation light sheet. *Opt. Express.* 23:6102–6111.
18. Dean, K. M., P. Roudot, …, R. Fiolka. 2015. Deconvolution-free subcellular imaging with axially swept light sheet microscopy. *Biophys. J.* 108:2807–2815.
19. Gao, L., L. Shao, …, E. Betzig. 2012. Noninvasive imaging beyond the diffraction limit of 3D dynamics in thickly fluorescent specimens. *Cell.* 151:1370–1385.
20. Shaner, N. C., M. Z. Lin, …, R. Y. Tsien. 2008. Improving the photostability of bright monomeric orange and red fluorescent proteins. *Nat. Methods.* 5:545–551.
21. Doyon, J. B., B. Zeitler, …, D. G. Drubin. 2011. Rapid and efficient clathrin-mediated endocytosis revealed in genome-edited mammalian cells. *Nat. Cell Biol.* 13:331–337.
22. Johnson, H. W., and M. J. Schell. 2009. Neuronal IP3 3-kinase is an F-actin-bundling protein: role in dendritic targeting and regulation of spine morphology. *Mol. Biol. Cell.* 20:5166–5180.
23. Liu, A. P., D. Loerke, …, G. Danuser. 2009. Global and local regulation of clathrin-coated pit dynamics detected on patterned substrates. *Biophys. J.* 97:1038–1047.
24. Welf, E. S., S. Ahmed, …, J. M. Haugh. 2012. Migrating fibroblasts reorient directionality by a metastable, PI3K-dependent mechanism. *J. Cell Biol.* 197:105–114.
25. Huisken, J., and D. Y. R. Stainier. 2007. Even fluorescence excitation by multidirectional selective plane illumination microscopy (mSPIM). *Opt. Lett.* 32:2608–2610.
26. Botcherby, E. J., R. Juskaitis, …, T. Wilson. 2007. Aberration-free optical refocusing in high numerical aperture microscopy. *Opt. Lett.* 32:2007–2009.
27. Botcherby, E. J., C. W. Smith, …, T. Wilson. 2012. Aberration-free three-dimensional multiphoton imaging of neuronal activity at kHz rates. *Proc. Natl. Acad. Sci. USA.* 109:2919–2924.
28. Keller, P. J., A. D. Schmidt, …, E. H. K. Stelzer. 2008. Reconstruction of zebrafish early embryonic development by scanned light sheet microscopy. *Science.* 322:1065–1069.
29. Haugh, J. M., F. Codazzi, …, T. Meyer. 2000. Spatial sensing in fibroblasts mediated by 3′ phosphoinositides. *J. Cell Biol.* 151:1269–1280.
30. Innocenti, M., E. Frittoli, …, G. Scita. 2003. Phosphoinositide 3-kinase activates Rac by entering in a complex with Eps8, Abi1, and Sos-1. *J. Cell Biol.* 160:17–23.
31. Deming, P. B., S. L. Campbell, …, A. K. Howe. 2008. Protein kinase A regulates 3-phosphatidylinositide dynamics during platelet-derived growth factor-induced membrane ruffling and chemotaxis. *J. Biol. Chem.* 283:35199–35211.

32. Gao, X., D. Xing, …, Y. Tang. 2009. H-Ras and PI3K are required for the formation of circular dorsal ruffles induced by low-power laser irradiation. *J. Cell. Physiol.* 219:535–543.

33. Burnette, D. T., S. Manley, …, J. Lippincott-Schwartz. 2011. A role for actin arcs in the leading-edge advance of migrating cells. *Nat. Cell Biol.* 13:371–381.

34. Liu, Y.-J., M. Le Berre, …, M. Piel. 2015. Confinement and low adhesion induce fast amoeboid migration of slow mesenchymal cells. *Cell.* 160:659–672.

35. Lorentzen, A., J. Bamber, …, C. J. Marshall. 2011. An ezrin-rich, rigid uropod-like structure directs movement of amoeboid blebbing cells. *J. Cell Sci.* 124:1256–1267.

36. Welf, E. S., and G. Danuser. 2014. Using fluctuation analysis to establish causal relations between cellular events without experimental perturbation. *Biophys. J.* 107:2492–2498.

37. Vilela, M., N. Halidi, …, G. Danuser. 2013. Fluctuation analysis of activity biosensor images for the study of information flow in signaling pathways. *Methods Enzymol.* 519:253–276.

38. Boulant, S., C. Kural, …, T. Kirchhausen. 2011. Actin dynamics counteract membrane tension during clathrin-mediated endocytosis. *Nat. Cell Biol.* 13:1124–1131.

39. Yuan, T., L. Liu, …, L. Chen. 2015. Diacylglycerol guides the hopping of clathrin-coated pits along microtubules for exo-endocytosis coupling. *Dev. Cell.* 35:120–130.

40. Kural, C., A. A. Akatay, …, T. Kirchhausen. 2015. Asymmetric formation of coated pits on dorsal and ventral surfaces at the leading edges of motile cells and on protrusions of immobile cells. *Mol. Biol. Cell.* 26:2044–2053.

41. Jaqaman, K., D. Loerke, …, G. Danuser. 2008. Robust single-particle tracking in live-cell time-lapse sequences. *Nat. Methods.* 5:695–702.

42. Aguet, F., C. N. Antonescu, …, G. Danuser. 2013. Advances in analysis of low signal-to-noise images link dynamin and AP2 to the functions of an endocytic checkpoint. *Dev. Cell.* 26:279–291.

43. Danuser, G. 2014. Reply to "Acquisition frame rate affects microtubule plus-end tracking analysis". *Nat. Methods.* 11:220.

44. Discher, D. E., D. J. Mooney, and P. W. Zandstra. 2009. Growth factors, matrices, and forces combine and control stem cells. *Science.* 324:1673–1677.

45. Pickup, M. W., J. K. Mouw, and V. M. Weaver. 2014. The extracellular matrix modulates the hallmarks of cancer. *EMBO Rep.* 15:1243–1253.

46. Butcher, D. T., T. Alliston, and V. M. Weaver. 2009. A tense situation: forcing tumour progression. *Nat. Rev. Cancer.* 9:108–122.

47. Fahrbach, F. O., F. F. Voigt, …, J. Huisken. 2013. Rapid 3D light-sheet microscopy with a tunable lens. *Opt. Express.* 21:21010–21026.

48. Olarte, O. E., J. Andilla, …, P. Loza-Alvarez. 2015. Decoupled illumination detection in light sheet microscopy for fast volumetric imaging. *Optica.* 2:702.

49. Abrahamsson, S., U. Satoru, and T. Wilson. 2006. A new approach to extended focus for high-speed, high-resolution biological microscopy. *In* Proceedings of SPIE. J.-A. Conchello, C. J. Coqswell, and T. Wilson, editors. International Society for Optics and Photonics.

50. Dean, K. M., and A. E. Palmer. 2014. Advances in fluorescence labeling strategies for dynamic cellular imaging. *Nat. Chem. Biol.* 10:512–523.

Biophysical Journal, Volume *110*

Supplemental Information

Diagonally Scanned Light-Sheet Microscopy for Fast Volumetric Imaging of Adherent Cells

Kevin M. Dean, Philippe Roudot, Carlos R. Reis, Erik S. Welf, Marcel Mettlen, and Reto Fiolka

Biophysical Journal

Supporting Material

Diagonally Scanned Light-Sheet Microscopy for Fast Volumetric Imaging of Adherent Cells

Kevin M. Dean,[1,2] Philippe Roudot,[1,2] Carlos R. Reis,[2] Erik S. Welf,[1,2] Marcel Mettlen,[2] and Reto Fiolka[2,*]

[1]Lyda Hill Department of Bioinformatics and [2]Department of Cell Biology, University of Texas Southwestern Medical Center, Dallas, Texas

*Correspondence: reto.fiolka@utsouthwestern.edu

Supporting Figures:

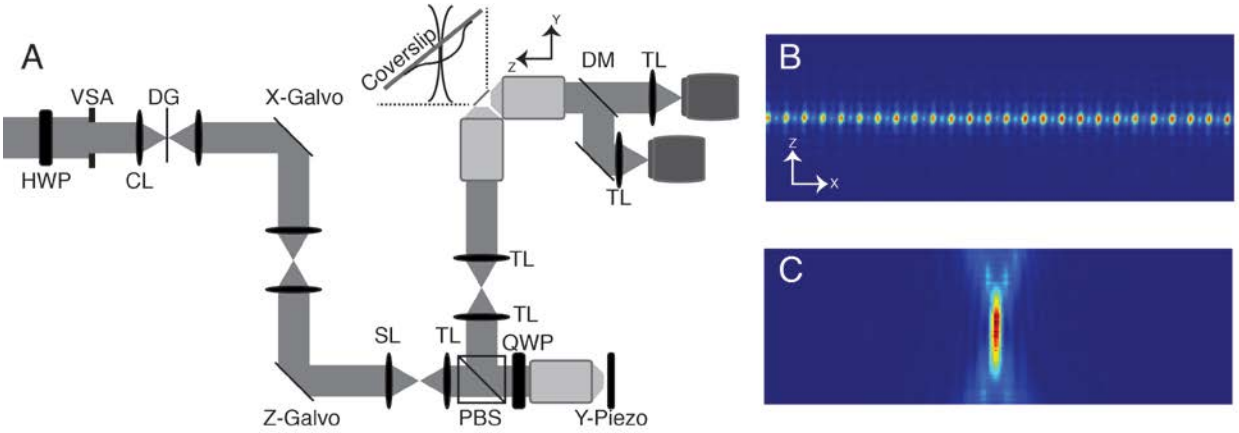

Figure S1. (A) Technical drawing of microscope. HWP: half-waveplate, VSA: variable slit aperture, CL: cylindrical lens, DG: diffraction grating, SL: scan lens, TL: tube lens, PBS: polarizing beam splitter, QWP: quarter wave plate, DM: dichroic mirror. The coverslip, oriented at 45 degrees, is placed at the focal plane of both the excitation and detection objectives. Magnified view provides orientation of coverslip and cell within the context of the overall microscope design. (B) Gaussian lattice as observed in the intermediate image plane between the remote and excitation objective. (C) Axial cross-section, summed over one period, of the Gaussian lattice.

v

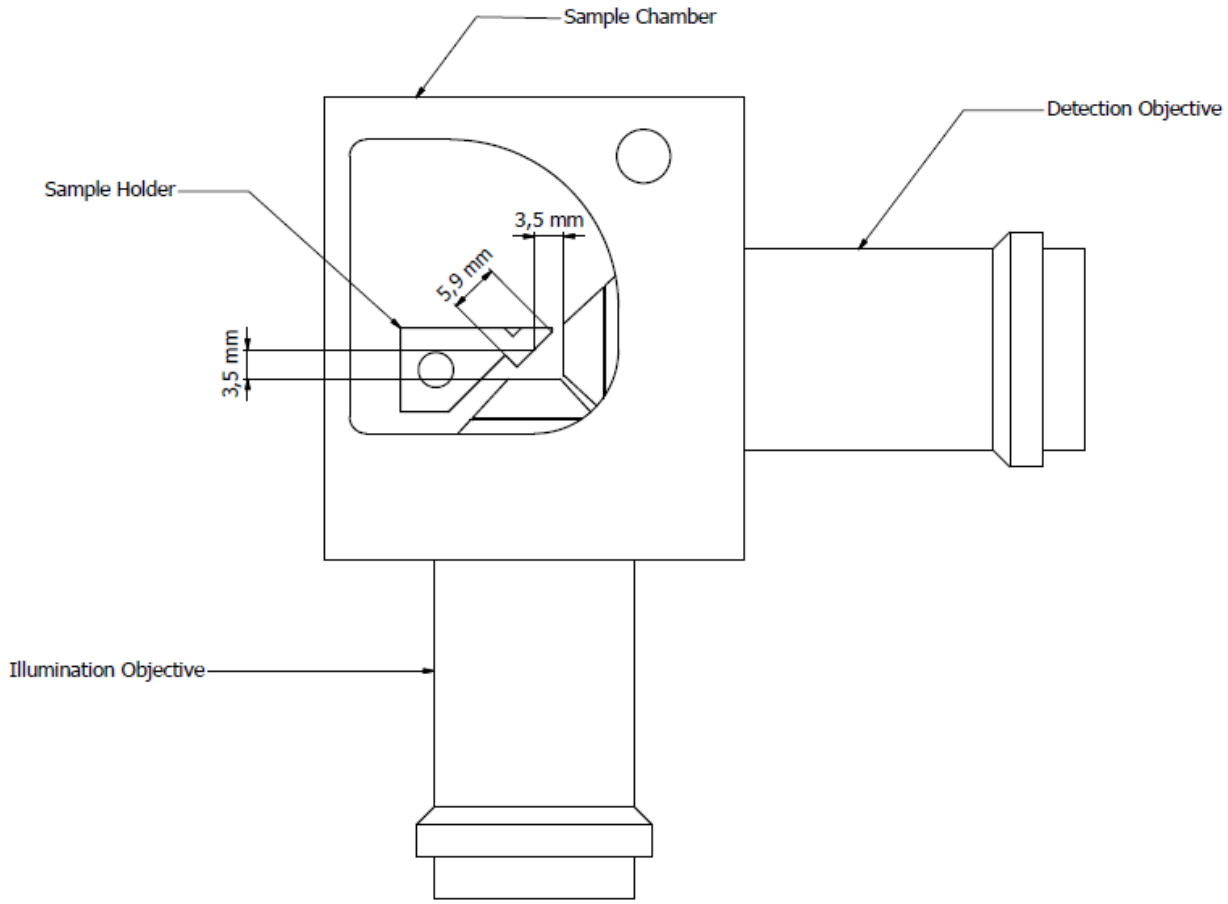

Figure S2. CAD drawing of the sample mounting inside the sample chamber and clearance to the illumination and detection objective.

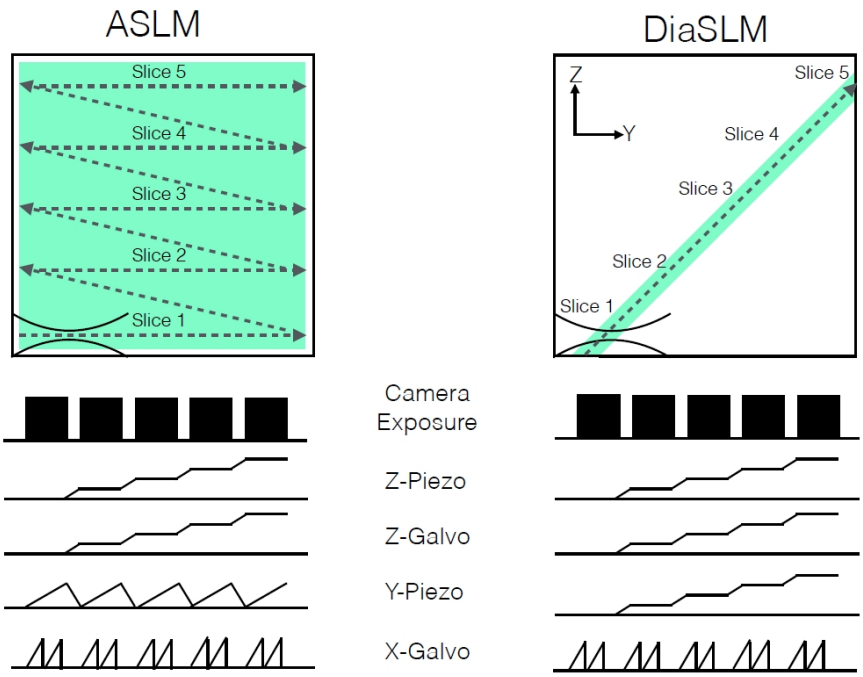

Figure S3. Schematic comparison of the beam scanning and camera control for ASLM and DiaSLM. In DiaSLM, the Y-piezo makes one complete cycle per image volume. In ASLM, the Y-piezo makes one complete cycle per image plane. Diagrams not to scale.

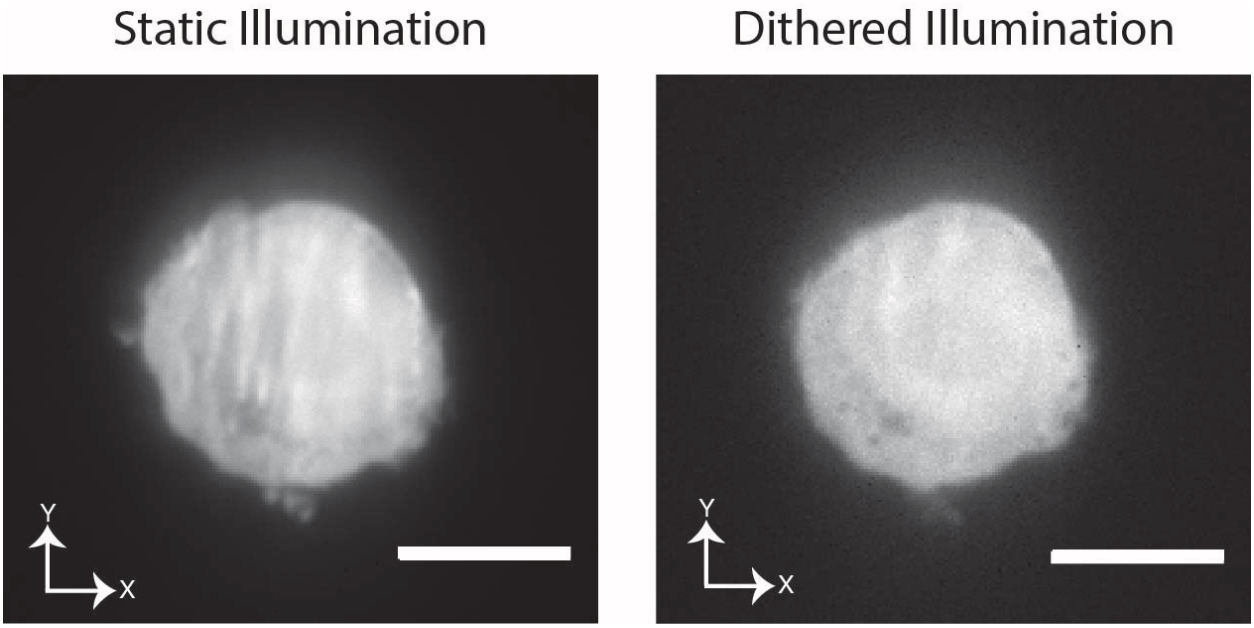

Figure S4. Improvement of illumination homogeneity by dithered Gaussian lattice. (Left) Static Gaussian illumination of an MV3 cell labeled with cytosolic GFP. (Right) Dithered Gaussian lattice illumination of the same cell. Scale bar 10 μm.

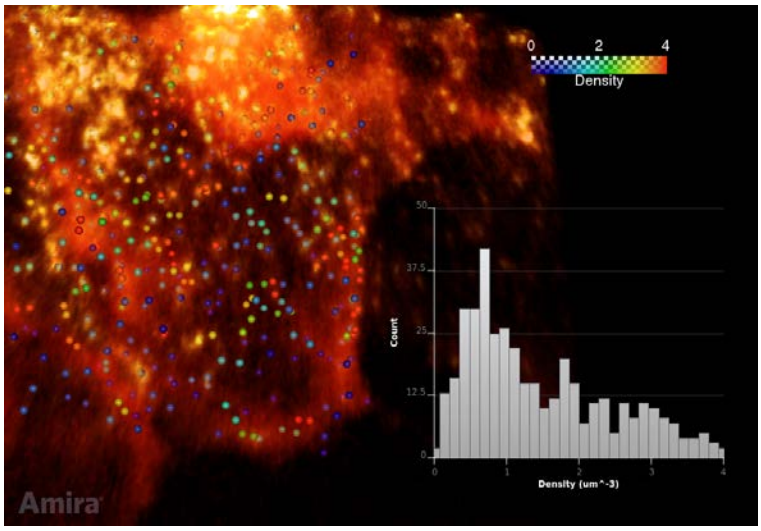

Figure S5. Density histogram (lower right), and locally measured density for each detected CLCa particle. The set of detected objects cover a volume of ~20x20x6 µm large.

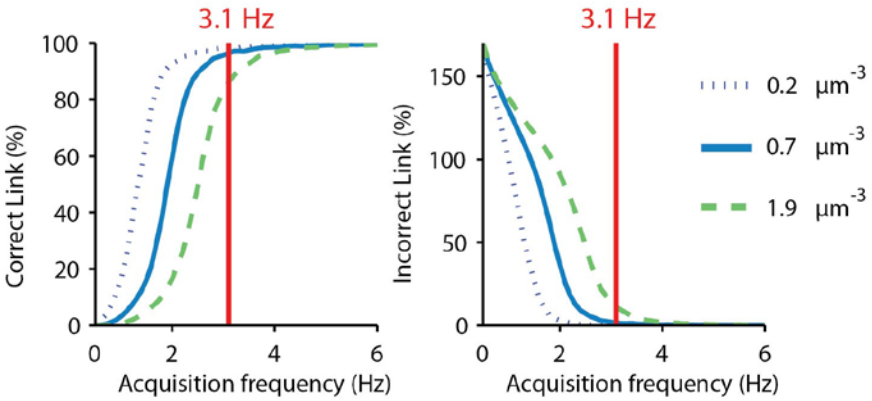

Figure S6. Tracking performance as a function of volumetric acquisition frequency on simulated dynamics of fast clathrin-associated structures (>2.22 µm/s) in a population of particles that simulate the density at the membrane (0.72 object per μm^3). Performance is measured on tracks undergoing active transport only. Percentages are relative to the true number of correct links.

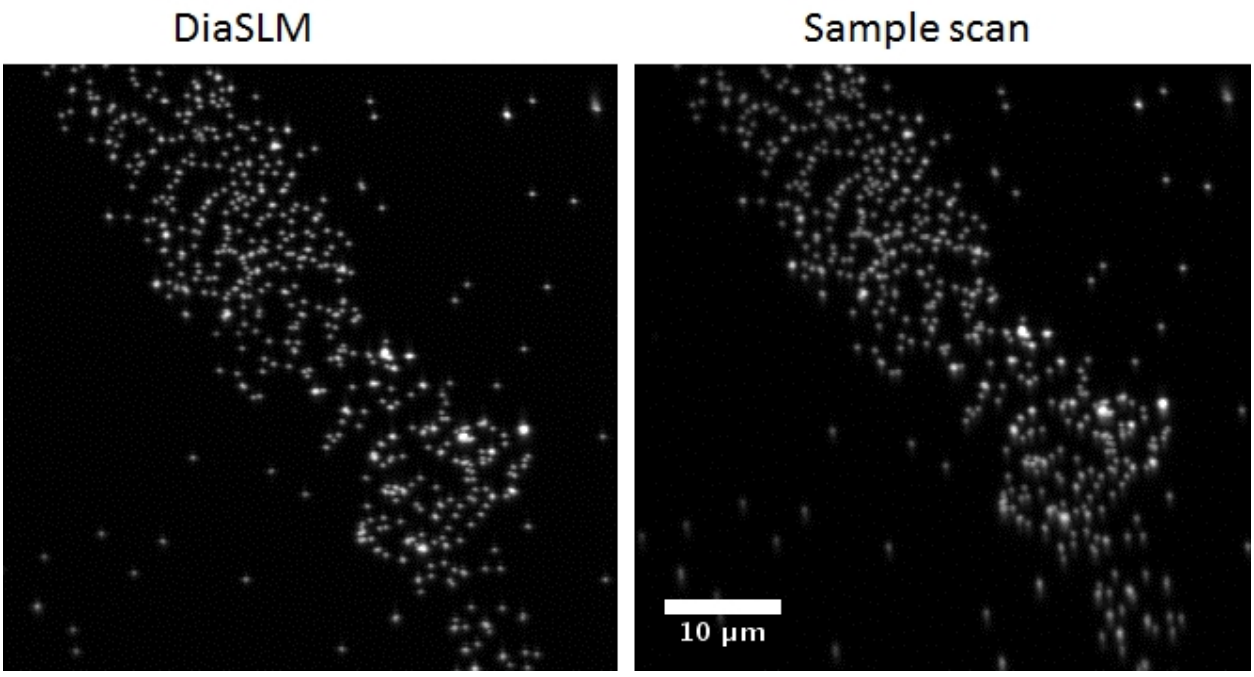

Figure S7. Comparison of DiaSLM and sample scanning. 200 nm fluorescent nanospheres were adhered to glass coverslips, and imaged with a 5 ms exposure time with (Left) DiaSLM and (Right) sample scanning. The two XZ images look comparable, except for the lower part of the sample scan image where the beads are slightly enlarged in the Z direction. However, the large scale oscillations that can be observed in the collagen imaging using sample scanning are not present.

Supporting Movies:

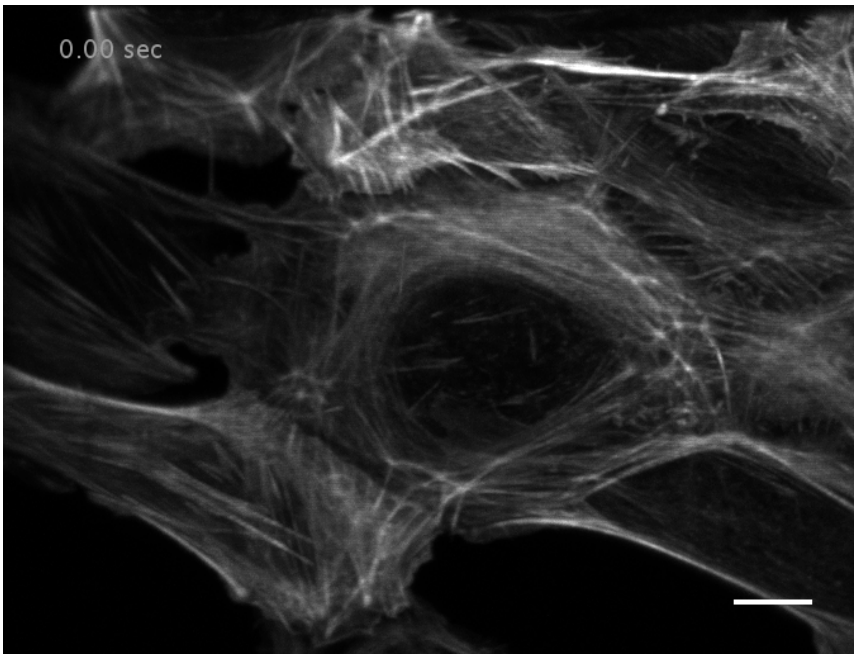

Movie S1. XY maximum intensity projection of F-actin dynamics in a monolayer of U2OS osteosarcoma cells, labeled with Tractin-CyOFP. Volumetric image acquisition rate of 0.37 Hz, 500 time points, 10 ms image acquisition per plane. Horizontal striping visible in the movie is likely due to laser intensity fluctuations. Scale bar 10 μm.

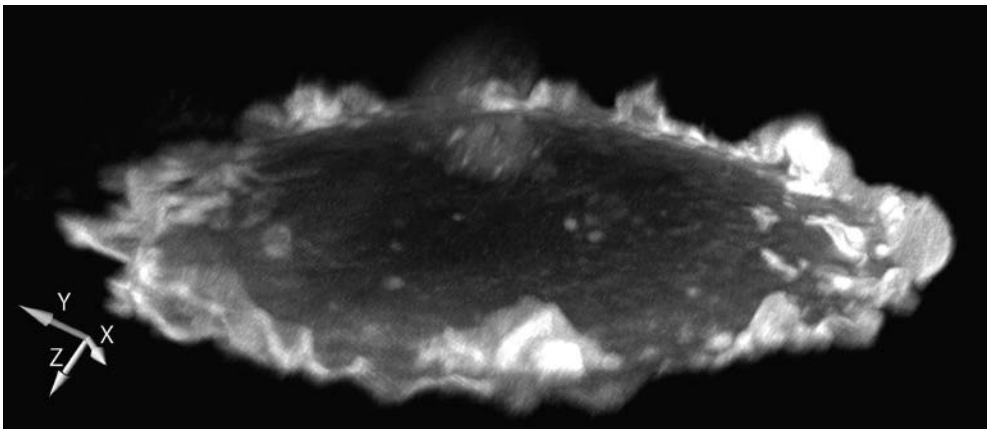

Movie S2. Volume rendering of a MV3 melanoma cell undergoing dynamic membrane ruffling, with enhanced phosphatidylinositol present in active membrane ruffles. Volumetric image acquisition rate of 0.37 Hz., 158 time points, 5 ms image acquisition per plane.

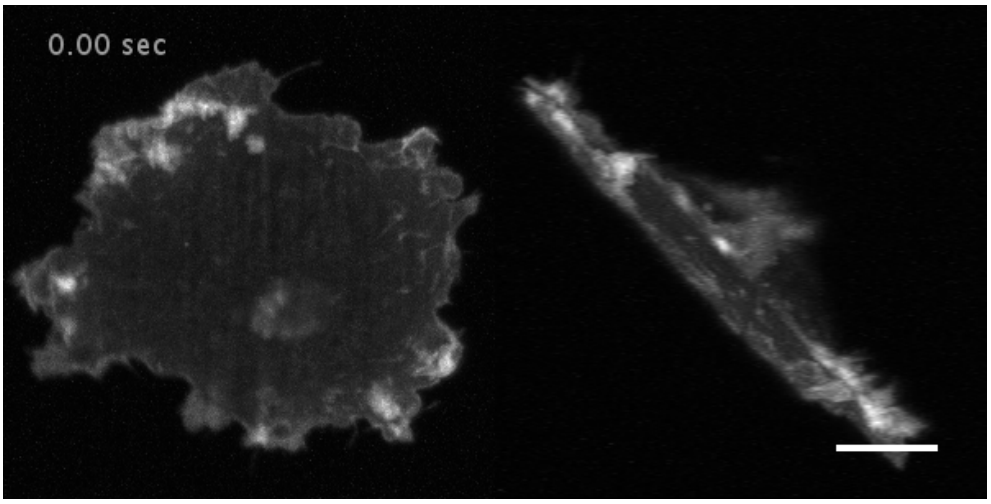

Movie S3. XY and ZY maximum intensity projections of an MV3 cell expressing AktPH-GFP. Volumetric image acquisition rate of 1 Hz, 500 time points, 5 ms image acquisition per plane. Scale bar 10 μm.

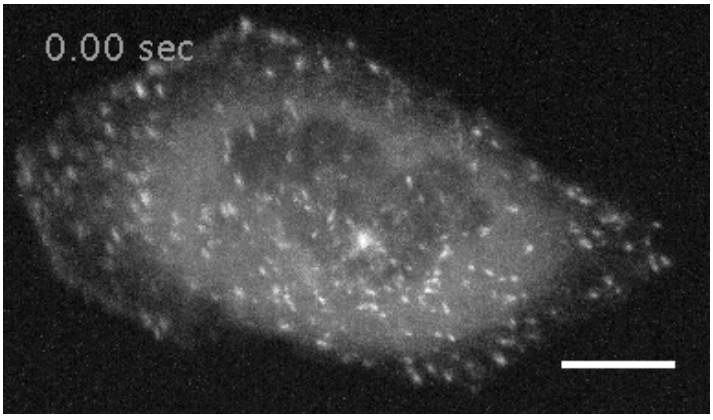

Movie S4. XY maximum intensity projection of microtubule +TIPs, labeled with EB3-mNeonGreen, in an osteosarcoma U2OS cell. Exponential photobleaching correction applied. Volumetric image acquisition rate of 0.46 Hz, 200 time points, 20 ms image acquisition per plane. Scale bar 10 μm.

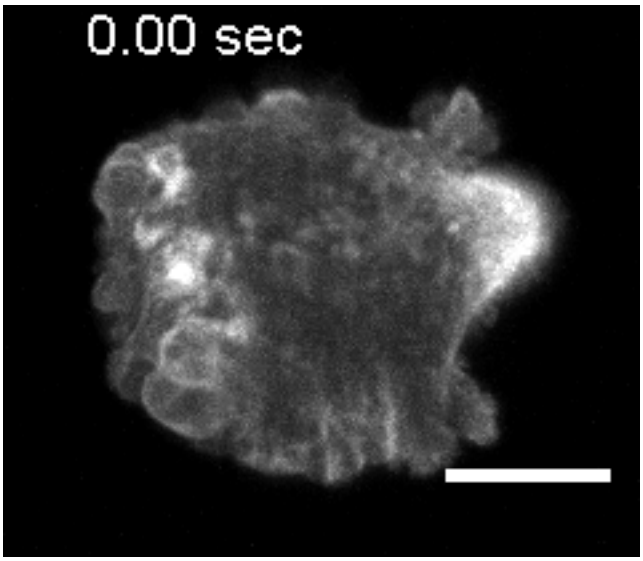

Movie S5. Polarized blebbing in a MV3 melanoma cell. XY maximum intensity projection of F-actin cytoskeleton imaged with Tractin-GFP. Volumetric image acquisition rate of 2.85 Hz., 1000 time points, 2.5 ms image acquisition per plane. Scale bar 10 μm.

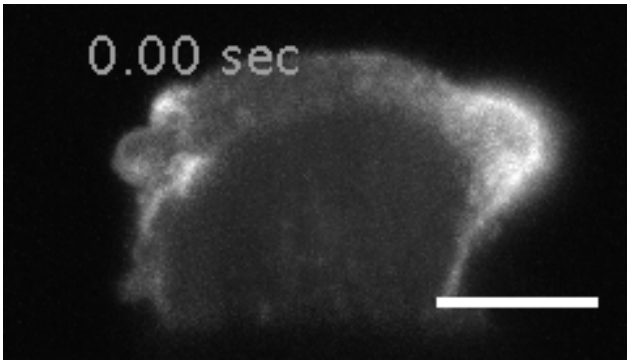

Movie S6. Cortical flow in polarized blebbing. Displayed as a local maximum intensity projection encompassing the central 4 μm of the cell. Same cell as in Movie S5. Volumetric image acquisition rate of 2.85 Hz., 1000 time points, 2.5 ms image acquisition per plane. Scale bar 10 μm.

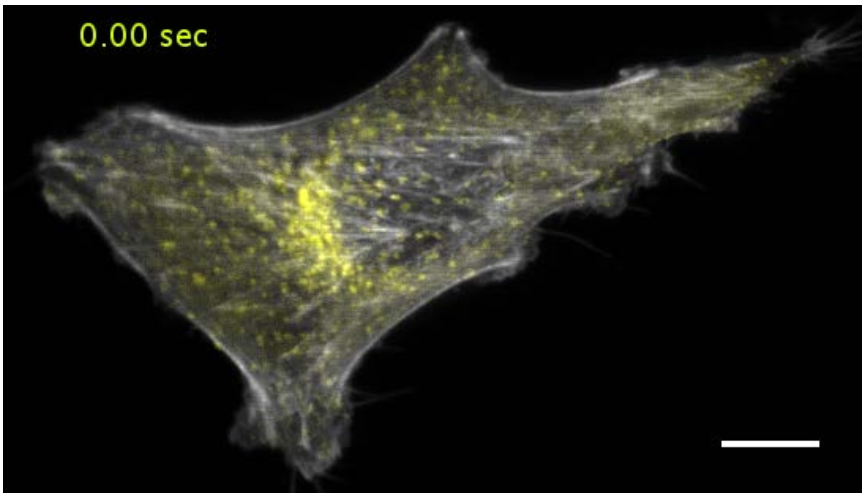

Movie S7. Clathrin-mediated endocytosis (yellow) and actin cytoskeleton (gray) dynamics in an SK-MEL2 melanoma cell. XY maximum intensity projection of clathrin light chain A (CLCa) marks active sites of endocytosis at the plasma membrane, and also labels intracellular structures associated with the Golgi apparatus, clearly visible in the perinuclear region of the cell. Each color channel acquired sequentially. Volumetric image acquisition rate of 0.20 Hz, 223 time points, 20 ms image acquisition per plane. Scale bar 10 μm.

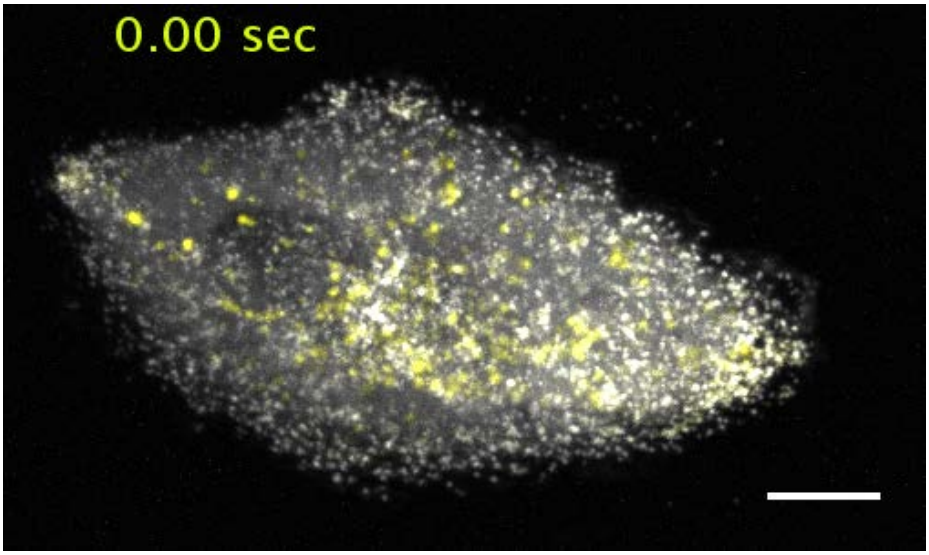

Movie S8. XY maximum intensity projection of clathrin-mediated endocytosis (gray) and transferrin (yellow) uptake and intracellular transport in a human retinal pigment epithelial (ARPE-19) cell. Color channels are acquired simultaneously. Volumetric image acquisition rate of 0.36 Hz., 500 time points, 20 ms image acquisition per plane. Scale bar 10 μm.

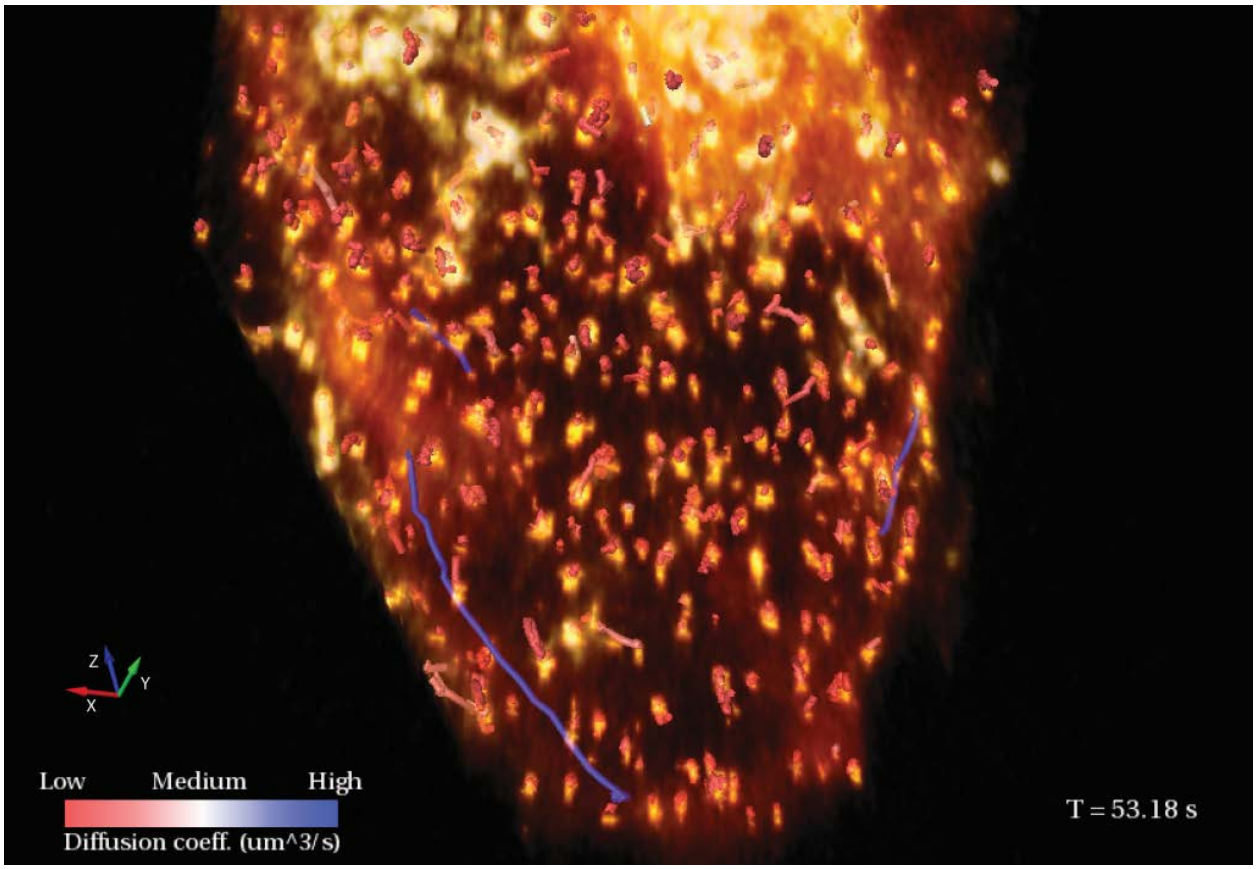

Movie S9. 3D particle tracking of clathrin associated structures in Caco-2 human colon carcinoma cells at 3.5 Hz volumetric acquisition rate. The vast majority of tracks show a confined displacement at the membrane and thus exhibit a low diffusion coefficient (red colored tracks). Rare events of active translocations can be detected with a maximum velocity 4.5 μm/s (shown in blue).

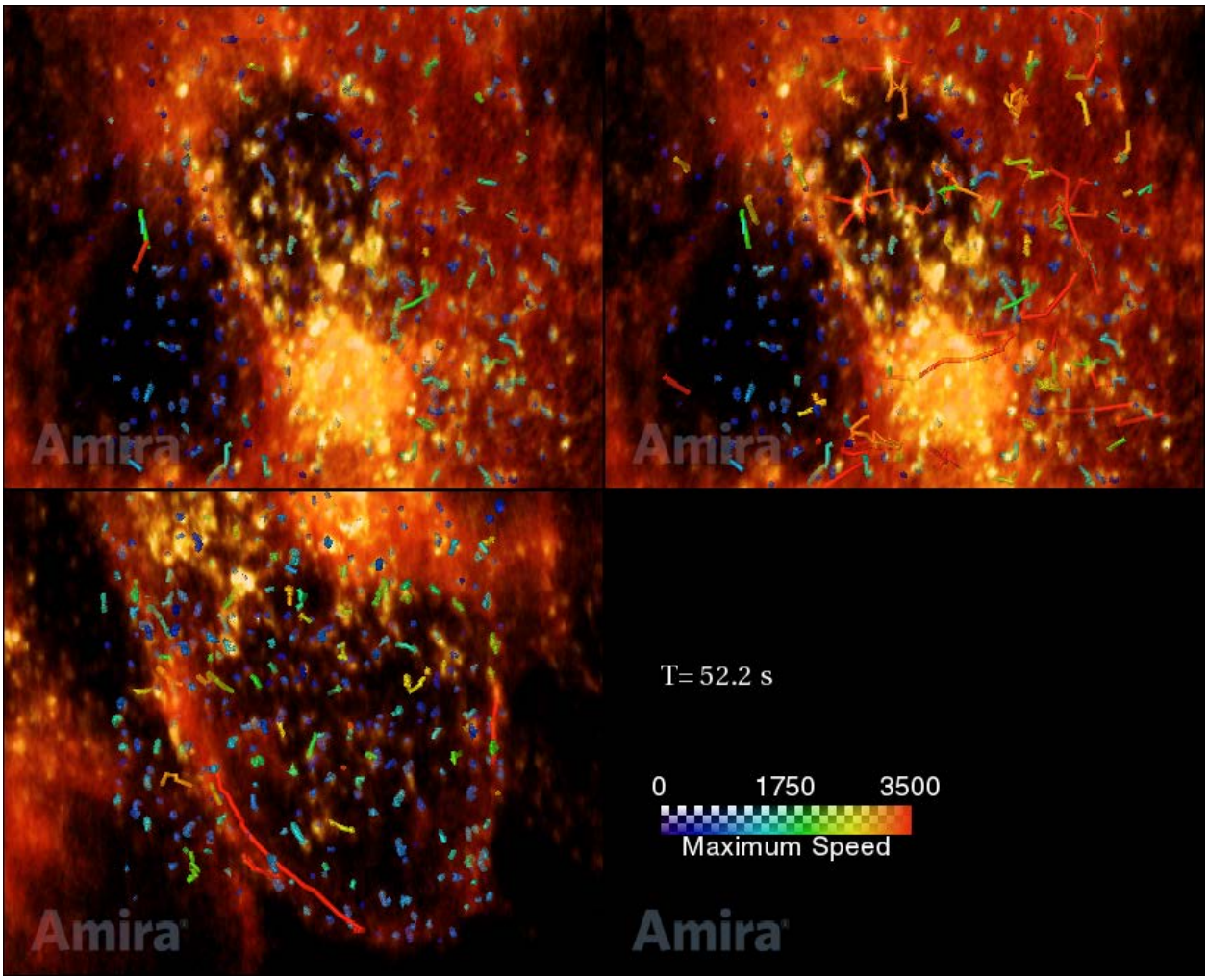

Movie S10: A minimum volumetric image acquisition rate of 3.1 Hz is necessary to accurately track 4.5 μm/s motion. Upper left, 2.2 Hz sequence tracked with a maximum search radius of 1.8 μm/s. Upper right: 2.2 Hz sequence tracked with a maximum search radius of 2.8 μm/s. Lower left: 3.5 Hz sequence tracked with a maximum search radius of 2.8 μm/s.

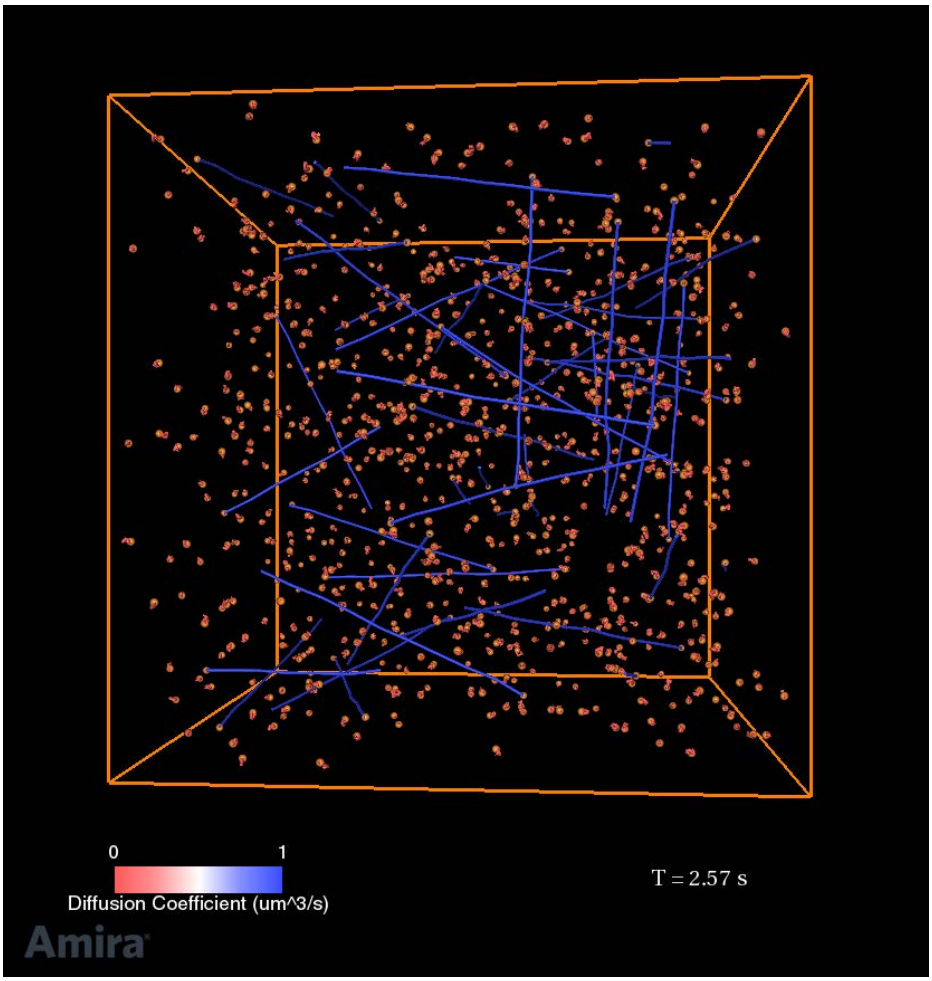

Movie S11: An example of simulated dynamics of intracellular clathrin-associated structures at the membrane (density is 0.72 object per μm^3). Tracks are pseudocolored using their estimated diffusion coefficient (red tracks are below 0.5 $\mu m^3/s$). Orange bounding box is 60x60x60 μm^3.

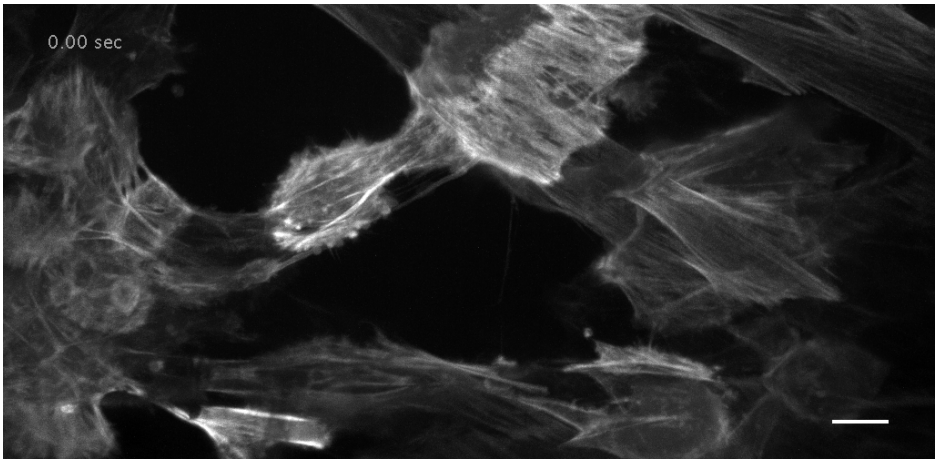

Movie S12. Human bronchial epithelial cells on a 50:50 extracellular matrix consisting of matrigel and type II collagen, 1 mg/mL. XY maximum intensity projection of cells labeled with Tractin-GFP. Volumetric image acquisition rate of 0.17 Hz., 500 time points, 10 ms image acquisition per plane. Scale bar 10 μm. Data has been subjected to image registration to account for movement of the sample using the ImageJ function StackReg.

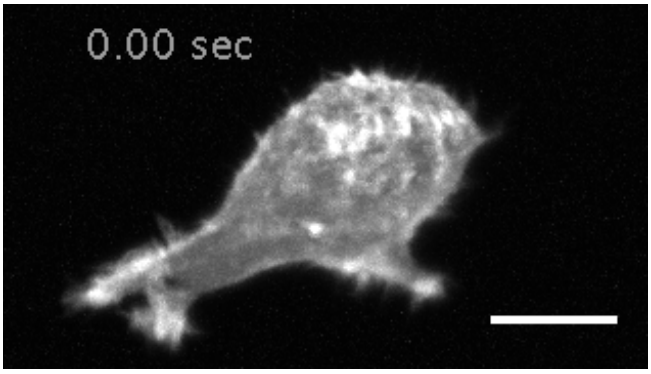

Movie S13. XY maximum intensity projection of human osteosarcoma U2OS cell undergoing cell spreading on a 2 mg/mL collagen matrix. Volumetric image acquisition rate of 1.37 Hz., 3000 time points, 2 ms image acquisition per plane.

Supporting Material

Supporting Note 1: 3D particle tracking.

The particle tracking approach is very similar to the one used in our previous report (1). We use the 3D version of the detector introduced by Auget *et al.* (2) and combine it with the u-track algorithm (3). A notable difference is the use of a multiple motion model to handle both confined Brownian displacement and directed displacement with multiple Kalman filters that compete with each other. Below are the parameters used for the tracking associated to the linking and the gap closing functions, respectively. The maximum search radius is set in voxels (normalized to the lateral voxel size), which was 800 or 1280 nm, depending on the experiment.

'costMatRandomDirectedSwitchingMotionLink'		**'costMatRandomDirectedSwitchingMotionCloseGaps'**	
LinearMotion	1	timeWindow	1
minSearchRadius	3	mergeSplit	0
maxSearchRadius	5 (or 8)	minTrackLen	3
brownStdMult	6	LinearMotion	0
useLocalDensity	0	minSearchRadius	2
nnWindow	timeWindow	maxSearchRadius	5
kalmanInitParam	[ ]	brownStdMult	6*timeWindow
		brownScaling	[0.25 0.01]
		ampRatioLimit	[0.7 4]
		LenForClassify	5
		useLocalDensity	0
		nnWindow	timeWindow
		maxAngleVV	[ ]
		gapPenalty	1.5

Supporting Note 2: Validation of acquisition frequency requirement with numerical simulations.

In order to cross-validate our experimental data showing the impact of volumetric acquisition frequency on automated tracking reliability (see Movie S10), we simulated imaging of intracellular transport in a dense environment. The synthetic dynamics reflect the active transport measured in our experimental datasets of clathrin vesicles (see Movie S11). As such, the population of synthetic particles undergoes active motions with a minimum speed of 2.2 μm/s in a dense field of locally confined diffusing particles. Acceleration is not simulated for the sake of simplicity. Consequently, the velocities of actively transported structures are modeled as stationary with an additional Brownian component. In our numerical experiments, we tune the frequency of acquisition and the particle density to evaluate automated tracking performance. The parameterization of our simulations is as follows:

- Volume: 100x100x100 μm
- Density: 0.1 to 4 particle/μm^3
- Active transport speed: 2.2 μm/s
- Active transport Brownian component: 0.01 $\mu m^3/s$
- Volume acquisition frequency : 1 to 6 Hz
- Confined motion proportion: 80%
- Active transport: 20%
- Frame number: 150
- Lifetime: follows a normal distribution with a mean and standard deviation of 10 and 25 seconds, respectively.
- Diffusion coefficient: 0.01 $\mu m^3/s$
- Confined radius: 0.3 to 0.8 μm (randomly distributed)

The parameters of the tracking algorithm are the same as in Note 1. The only difference is the upper bound of the frame-to-frame assignment radius (parameter maxSearchRadius) which adapts to the volumetric acquisition frequency from 2,200 nm/frames (for 1 Hz) down to 370 nm/frame (for 6 Hz). This provides us with a ground truth and a measured set of tracks with a finely tuned parameterization. By measuring the number of correct and wrong links estimated by the tracker and focusing on the directed displacement, we can evaluate the dynamic resolution of the simulated system in a systematic fashion.

To interrogate the impact of density and volumetric acquisition frequency on automated tracking performance, we simulated 12 different samples with intracellular densities ranging from 0.1 to 4 particles per volume. Fig. 5C shows that active transport of clathrin-associated structures cannot be reliably quantified below 3 Hz, even in the sparser scenario. These data also clearly show the large gap in efficiency between 2 Hz and 3 Hz.

We then tested the predictive power of our theoretical model (see Note 3) by simulating the median particle density measured at the membrane in our experimental sample (0.72 objects per μm^3) and measured the tracking performance against the acquisition frequency (see Fig. S7). As predicted by our model, the percentage of correct and incorrect links asymptotically reaches 100% and 0%, respectively, at a volumetric image acquisition frequency of ~ 3.1 Hz tracking. Fig. S7 also shows the impact of lower

acquisition frequencies on the measurements of particle dynamics for a specific density. At an image acquisition frequency of 2 Hz, the tracking quality deteriorates to 20%, underscoring the importance of high-speed 3D microscopes. These data also show that high particle densities (*e.g.*, adjacent to the Golgi apparatus) hinders particle tracking quality, suggesting that even faster microscopes may be needed for specific applications.

Supporting Note 3: Relationship between volumetric acquisition frequency and quantification of rapid intracellular transport.

For the quantification of rapid intracellular dynamics, it is intuitive that high frequency three-dimensional imaging is critical. However, it is currently unclear what improvements are required to capture the speeds and heterogeneity present in intracellular processes. In this supplemental note, we provide a simple model to estimate the required spatiotemporal resolution for a given acquisition setup for Brownian and directed displacement using state-of-the-art tracking techniques.

A typical tracking algorithm first detects particles in multiple image volumes, and then links the detected particles in a set of coherent tracks (4). If the apparent per-frame displacement of an object is fast and in a crowded environment, ambiguities arise in (i) the association of valid detections in neighboring trajectories, (ii) the inference of transient detection loss, (iii) the inference of false positives in the detection set, and (iv) the estimation of track termination and initiation. In an attempt to solve these problems, one strategy commonly used is to estimate the speed gating parameter, or "search radius" S(t), which defines the maximum distance possible for one detected particle to be linked to another detected particle in the next frame. This parameter can be learned for each track, and adapted to accommodate new frames. However, it is usually saturated by a maximum value in an effort to avoid false positive links induced by the above-mentioned ambiguities (3, 4). Ideally, to allow for transient misdetection and spontaneous track initiation/termination, the sphere described by this search radius has a particle density below 1:

$$\frac{4}{3}\pi S(t)^3 d(t) < 1$$

where d(t) is the local density. Obviously, this sphere should also contain all the possible motion of the object of interest. In the case of a freely diffusing particle we thus have:

$$\frac{v(t)}{f} < S(t)$$

where v is the instantaneous speed and f is the acquisition frequency. We can thus link the speed, acquisition speed and density with:

$$\frac{4}{3}\pi\left(\frac{|v(t)|}{f}\right)^3 d(t) < 1. \quad (1)$$

And the speed that can be estimated for given frequency and density:

$$|v| < f\sqrt[3]{\frac{3}{4\pi d(t)}}.$$

In the directed motion scenario, which is the most challenging in the CLCa experiment performed, an additional layer of complexity is added by the predictive capacity of Kalman filtering. After a first link, the Kalman filter estimates the trajectory

speed, allowing for a prediction of the particle location in the next frame. This prediction is then used for linking against candidate neighboring detection. U-track performs three tracking passes to estimate this speed. In turn, this means that condition (1) applies on the minimum speed of the track only, as far as the trajectories follow a quasi-stationary speed. Modeling speed variation through instantaneous acceleration a, directed transport is subject to the additional constraint:

$$\frac{4}{3}\pi\left(\frac{|a|}{f^2}\right)^3 d(t) < 1.$$

For a given density, the imaging frequency has a quadratic impact on the measurable acceleration.

Measuring local density on our experimental data, we can thus predict the speed attainable for a given acquisition frequency or, more importantly, knowing what acquisition frequency is required for a given magnitude of intracellular transport. Estimating local density according to the distance to the nearest neighbor, we find generally two modes: one at 0.72 object/μm^3 for sparser area and 1.9 object/μm^3 in the denser area, such as the Golgi apparatus (see also Fig. S6). This implies that for a conventional algorithm, an acquisition rate of 3.5 Hz should be able to capture speeds of up to 2.4 μm/s in the Brownian case in the sparser area. As for directed transport, an acquisition rate of 3.5 Hz would enable us to reliably track trajectories that present a minimum speed of 2.4 μm/s and instantaneous acceleration of 8.6 $\mu m/s^2$. Using an adaptive search radius that saturates at 800 nm/frame (2.8 μm/s), we can indeed measure directed motions as rapid as 4.5 μm/s (see Fig. 5A and 5B) with our setup. The longest trajectory, on Fig. 5B, presents a minimum speed of 2.2 μm/s in its directed section.

Our model predicts that the fastest trajectory measured in Fig. 5A, presenting a minimum speed of 2.2 μm/s requires a minimum acquisition frequency of 3.1 Hz. In order to test the reliability of our model as well as verifying that our new microscope truly enables the capture of these displacements, we performed 2.3 Hz acquisition on the same cell type on the same day and under same conditions. While the SNR is noticeably better and thus detection more reliable, we observed a decrease in tracking quality. We performed automated tracking on this sequence using two different maximum search radius configurations. The first configuration saturates the search radius at 800 nm/frame, equivalent to a maximum speed of 1.8 μm/s in the Brownian case. The second configuration saturates at 1200 nm/frame, to match the maximum speed set by the search radius set in our 3.5 Hz experiment (2.8 μm/s). The upper left panel in Movie S10 shows that the first configuration generates very few false positives, but fails to detect the fast motion captured at the 3.5 Hz acquisition speed in the lower left panel. The second tracking configuration results in very fast tracks that are clearly not endocytic structures (*i.e.*, their movement is incoherent and physically unlikely). These results are confirmed by our model. Theoretically, we should not be able to measure objects that go faster than 1.54 μm/s in the Brownian case without false positives, and not be able to detect active transport are consistently above this speed and with acceleration above 3.4 $\mu m/s^2$. While trajectories that go as fast as 4.5 μm/s are in theory within reach, they should then accelerate up to three times their lowest speed, reducing the number of potential candidates. For example, tracks similar to the longest one detected in Fig. 5A are not detectable with such a setup.

Supporting References:

1. Dean, Kevin M., P. Roudot, Erik S. Welf, G. Danuser, and R. Fiolka. 2015. Deconvolution-free Subcellular Imaging with Axially Swept Light Sheet Microscopy. Biophysical Journal 108:2807-2815.
2. Aguet, F., Costin N. Antonescu, M. Mettlen, Sandra L. Schmid, and G. Danuser. 2013. Advances in Analysis of Low Signal-to-Noise Images Link Dynamin and AP2 to the Functions of an Endocytic Checkpoint. Developmental Cell 26:279-291.
3. Jaqaman, K., D. Loerke, M. Mettlen, H. Kuwata, S. Grinstein, S. L. Schmid, and G. Danuser. 2008. Robust single-particle tracking in live-cell time-lapse sequences. Nature Methods 5:695-702.
4. Chenouard, N., I. Smal, F. de Chaumont, M. Maska, I. F. Sbalzarini, Y. Gong, J. Cardinale, C. Carthel, S. Coraluppi, M. Winter, A. R. Cohen, W. J. Godinez, K. Rohr, Y. Kalaidzidis, L. Liang, J. Duncan, H. Shen, Y. Xu, K. E. Magnusson, J. Jalden, H. M. Blau, P. Paul-Gilloteaux, P. Roudot, C. Kervrann, F. Waharte, J. Y. Tinevez, S. L. Shorte, J. Willemse, K. Celler, G. P. van Wezel, H. W. Dan, Y. S. Tsai, C. Ortiz de Solorzano, J. C. Olivo-Marin, and E. Meijering. 2014. Objective comparison of particle tracking methods. Nat Methods 11:281-289.